




Mechanoregulation analysis of bone formation in tissue engineered constructs requires a volumetric method using time-lapsed micro-computed tomography

Journal Article

Author(s):

Griesbach, Julia K.; Schulte, Friederike A.; [Schädli, Gian Nutal](#) ; [Rubert, Marina](#) ; [Müller, Ralph](#) 

Publication date:

2024-04-15

Permanent link:

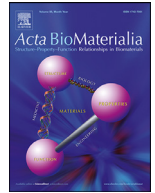
<https://doi.org/10.3929/ethz-b-000670479>

Rights / license:

[Creative Commons Attribution 4.0 International](#)

Originally published in:

Acta Biomaterialia 179, <https://doi.org/10.1016/j.actbio.2024.03.008>



Full length article

Mechanoregulation analysis of bone formation in tissue engineered constructs requires a volumetric method using time-lapsed micro-computed tomography

Julia K. Griesbach, Friederike A. Schulte, Gian Nutal Schädli, Marina Rubert, Ralph Müller*

Institute for Biomechanics, ETH Zürich, Gloriastrasse 37/39, 8092 Zürich, Switzerland

ARTICLE INFO

Article history:

Received 15 May 2023

Revised 9 February 2024

Accepted 7 March 2024

Available online 16 March 2024

Keywords:

Mechanoregulation

Finite element analysis

Tissue engineering

Micro-computed tomography

Bone

ABSTRACT

Bone can adapt its microstructure to mechanical loads through mechanoregulation of the (re)modeling process. This process has been investigated *in vivo* using time-lapsed micro-computed tomography (micro-CT) and micro-finite element (FE) analysis using surface-based methods, which are highly influenced by surface curvature. Consequently, when trying to investigate mechanoregulation in tissue engineered bone constructs, their concave surfaces make the detection of mechanoregulation impossible when using surface-based methods. In this study, we aimed at developing and applying a volumetric method to non-invasively quantify mechanoregulation of bone formation in tissue engineered bone constructs using micro-CT images and FE analysis. We first investigated hydroxyapatite scaffolds seeded with human mesenchymal stem cells that were incubated over 8 weeks with one mechanically loaded and one control group. Higher mechanoregulation of bone formation was measured in loaded samples with an area under the curve for the receiver operating curve ($AUC_{\text{formation}}$) of 0.633–0.637 compared to non-loaded controls ($AUC_{\text{formation}}$: 0.592–0.604) during culture in osteogenic medium ($p < 0.05$). Furthermore, we applied the method to an *in vivo* mouse study investigating the effect of loading frequencies on bone adaptation. The volumetric method detected differences in mechanoregulation of bone formation between loading conditions ($p < 0.05$). Mechanoregulation in bone formation was more pronounced ($AUC_{\text{formation}}$: 0.609–0.642) compared to the surface-based method ($AUC_{\text{formation}}$: 0.565–0.569, $p < 0.05$). Our results show that mechanoregulation of formation in bone tissue engineered constructs takes place and its extent can be quantified with a volumetric mechanoregulation method using time-lapsed micro-CT and FE analysis.

Statement of significance

Many efforts have been directed towards optimizing bone scaffolds for tissue growth. However, the impact of the scaffolds mechanical environment on bone growth is still poorly understood, requiring accurate assessment of its mechanoregulation. Existing surface-based methods were unable to detect mechanoregulation in tissue engineered constructs, due to predominantly concave surfaces in scaffolds. We present a volumetric approach to enable the precise and non-invasive quantification and analysis of mechanoregulation in bone tissue engineered constructs by leveraging time-lapsed micro-CT imaging, image registration, and finite element analysis. The implications of this research extend to diverse experimental setups, encompassing culture conditions, and material optimization, and investigations into bone diseases, enabling a significant stride towards comprehensive advancements in bone tissue engineering and regenerative medicine.

© 2024 The Author(s). Published by Elsevier Ltd on behalf of Acta Materialia Inc.
This is an open access article under the CC BY license (<http://creativecommons.org/licenses/by/4.0/>)

1. Introduction

Bone is a remarkable material known for its ability to functionally adapt its internal microarchitecture by bone (re)modeling to mechanical influences, which is called mechanoregulation. The

* Corresponding author.

E-mail address: ram@ethz.ch (R. Müller).

three main cells involved in bone (re)modeling are osteoblasts, which form bone, osteoclasts, which resorb bone, and osteocytes, which regulate this process. Mechanoregulation is a complex process that involves the activation of the Bone Genetic Regulatory Network in response to mechanical stimulation. A cascade of transcription factors, starting with RUNX2, is triggered when mechanical forces are exerted on bone tissue, such as through physical loading or exercise. One critical pathway involved in mechanoregulation is the WNT/beta-catenin pathway, which plays a crucial role in bone formation. The activation of mechanoregulation leads to a series of cellular responses, including the differentiation of mesenchymal stem cells into osteoblasts, increased production of bone extracellular matrix proteins, and enhanced mineralization. These events collectively contribute to the overall process of bone (re)modeling [1]. For a long time, the local sites of bone (re)modeling could only be analyzed and quantified using histomorphometry which is a destructive, and observer- and method-dependent method. Waarsing et al. proposed a 3-dimensional non-destructive method to identify areas of bone formation and resorption in living animals using time-lapsed micro-computed tomography (micro-CT) [2]. This process was extended by Schulte et al. who quantified local formation and resorption using principles of dynamic morphometry [3]. Using this concept, Schulte et al. [4] were able to associate (re)modeling events with the local mechanical environment obtained using micro-finite element (micro-FE) analysis. It was the first automated high throughput approach, that showed areas of high strain are associated with bone formation, while areas of low strain are associated with resorption. Their approach facilitated deeper preclinical investigations into mechanoregulation of bone (re)modeling [4] or fracture healing [5]. Scheuren et al. investigated mechanoregulation of trabecular bone adaptation at different loading frequencies [6], but found no significant differences, while Razi et al. showed the influence of aging on mechanoregulation on mouse bone (re)modeling [7].

The advances in non-destructive image-based mechanoregulation analysis also allowed the application to human bone [8], enabling insights into load distribution and direction [9,10]. Collins and Atkins et al. identified differences in mechanoregulation in human radii fractures between cohorts with different bone quality [11]. However, human clinical studies are challenging due to patient availability, lower image resolution, motion artefacts, and ethical concerns. Therefore, many recent efforts focus on tissue engineered constructs to investigate human bone biology and pathomechanisms to accompany or precede *in vivo* human research [12].

In vitro cultured tissue engineered constructs are emerging technologies with multiple potential applications. Bone scaffolds have been developed to facilitate fracture healing for large bone defects arising from complicated trauma or bone cancer [13–15]. To investigate a scaffold's osteogenic potential, *in vitro* studies often precede implantation in animal studies, mostly sheep and rodent models [16–18]. Scaffolds are usually seeded with human mesenchymal stromal cells (hMSCs) or human bone marrow-derived mesenchymal stromal cells *in vitro*, cultured in osteogenic medium and often subjected to mechanical stimulation, and the bone growth is monitored and evaluated using time-lapsed micro-CT imaging [13–15]. Additionally, there are *in vitro* bone organoids solely for research purposes to investigate organs in a controlled environment [19–21]. By using patient-derived cells, bone organoids have the potential to serve as personalized disease models to investigate pathomechanisms and personalized treatment options [22]. This offers new opportunities for research into rare diseases, like Osteogenesis Imperfecta [23].

Many efforts have been directed towards finding the optimal bone scaffold to enable bone tissue growth. It is well known that the micro-mechanical environment of the bone cells on the scaffold surface or within the scaffold influences the cell behav-

ior through mechanotransduction, which is affected by the material properties and scaffold geometry, such as pore size or shape and mechanical stimulation through e.g. compression or fluid flow [24,25]. As this is a complex process with many parameters, scaffold designs are nowadays often optimized using computational modeling of the mechanical environment and the cell behavior [26,27]. However, to optimize a scaffold regarding the mechanical environment, it must be well understood how this affects bone growth and to which extent mechanoregulation takes place *in vitro*.

Similarly to bone *in vivo*, mechanical stimulation has been shown to increase tissue formation in tissue engineered bone constructs [13,28–30] as well as tissue mineral density and scaffold stiffness [21]. Physiological deformation resulting in strain on osteoblastic cell lines in a 2D culture increases osteoprotegerin, a protein expressed by osteoblasts that inhibits osteoclastogenesis, while having no effect on RANKL, thus favoring bone formation [31]. Baas et al. [32] investigated the association of local mechanical stimuli with areas of tissue formation in a 3D scaffold using a manual approach, thus demonstrating mechanoregulation in tissue engineered bone constructs.

When applied to bone tissue engineered constructs for *in vitro* applications, our previously developed surface-based method [4] fails to detect mechanoregulation. Surface-based methods are highly influenced by the bone surface curvature as demonstrated by Young et al. [33]. Whereas human trabecular bone has mostly flat or convex surfaces [34], highly porous and concave surfaces are known to be beneficial to tissue growth in tissue engineered constructs, because adherent cells avoid convex regions during migration and position themselves in concave regions [35,36]. While (re)modeling takes place on the surface, mechanosensation and the formation and resorption process of bone is volumetric. We therefore assumed that a volumetric approach could be better suited to detect mechanoregulation in bone tissue engineered constructs.

Our goal was to investigate mechanoregulation of bone formation in tissue engineered constructs by developing a volumetric mechanoregulation assessment algorithm using time-lapsed micro-CT images from hMSC-seeded hydroxyapatite scaffolds with one mechanically loaded and one control group [13], image registration, and FE analysis. We assumed that the underlying mechanical signal influences the (re)modeling event, similar as in the surface-based method [4] and that osteocytes rather sense and communicate the highest effective strain than an average value [37]. We hypothesized that (I) mechanically loaded *in vitro* bone tissue engineered constructs show mechanoregulation in tissue formation, (II) mechanical loading increases mechanoregulation in tissue formation in tissue engineered constructs compared to non-loaded controls, and (III) the volumetric method is sensitive to changes and also applicable to *in vivo* mouse (re)modeling data that includes resorption from a previously published study [6].

2. Materials and methods

2.1. Surface-based mechanoregulation analysis

Our previously established surface-based mechanoregulation analysis [4] is based on a registered (re)modeling image identifying formation, resorption and quiescent bone [3], and the local mechanical environment derived from micro-FE simulations of the baseline (of the earlier time point) micro-CT scan. The challenge was to associate formation with the underlying mechanical environment. Since the mechanical environment is calculated with the baseline image, there is no tissue in the formation volume yet (see Fig. 1D,E and G,H). To associate the bone formation and resorption sites with the bone surface, formation and resorption volumes were projected onto the baseline scan surface using a 6-

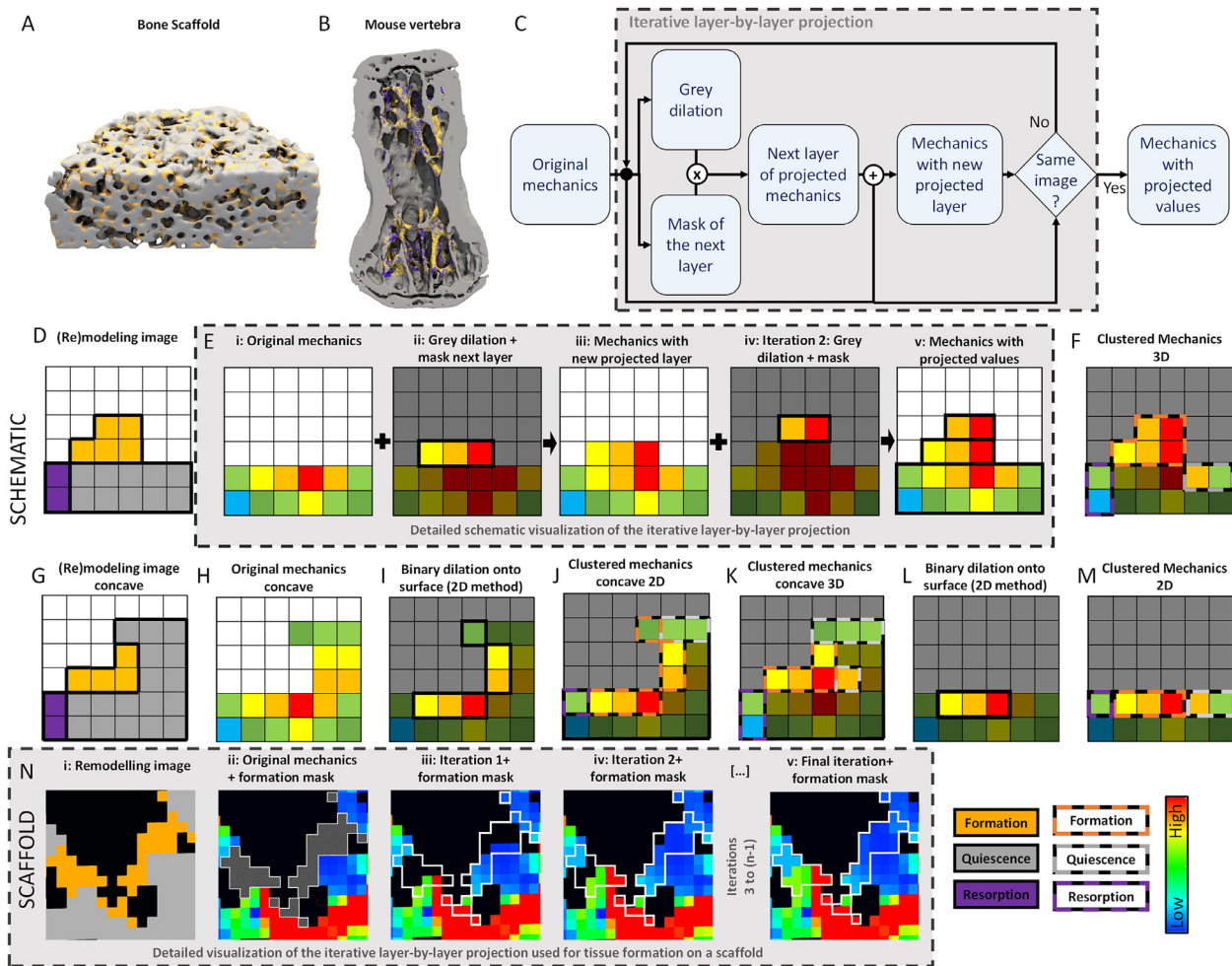


Fig. 1. Schematic of the volumetric projection method to assess mechanoregulation. A: 3D (re)modeling image of a bone scaffold. B: 3D (re)modeling image of a mouse vertebra. C: Schematic chart of the iterative layer-by-layer projection. D–F: Schematic of the projection of mechanical values at the surface: D: (Re)modeling image with multiple layers of formation. E: Iterative layer-by-layer projection of the surface values. F: Clustered mechanical values. G: (Re)modeling image of a concave surface. H: Corresponding mechanical environment to G). I: Binary dilation of the formation voxels onto the surface of the surface-based method. J: Clustered mechanical values of the concave image by the surface-based method. K: Clustered mechanical values for the concave surface by the volumetric method, L: Binary dilation of the formation voxels based on images D and Ei. M: Clustered mechanical values of the surface-based method based on images D and Ei. N: Example of a real close up of (re)modeling image and mechanical environment, where the iterative projection process is visually explained (not representative of the overall mechanoregulation).

neighborhood topology, meaning the 6 direct neighbors of a voxel in a hexagonal grid (Fig. 11, L). This resulted in three masks for the surfaces of each of the (re)modeling events, which are applied to the micro-FE image to obtain the clustered mechanical values for formation, quiescence and resorption (Fig. 1J, M).

The number of bins for the resulting formation, quiescence and resorption histograms was specified dependent on the application. We chose 50 bins for in the *in vivo* application, similar as in the original study [6], and 100 bins for the *in vitro* data, as there was roughly twice the amount of formation voxels compared to the *in vivo* data.

Projecting the formation onto the mechanical values at the adjacent surface of the formation does not capture mechanoregulation in predominantly concave structures such as bone scaffolds. The formation on concave surfaces inherently connects the formation voxel to multiple adjacent surfaces. Thus, the formation voxel is associated with multiple mechanical values (Fig. 11). Furthermore, the surface-based method fails to capture mechanoregulation, where large amounts of formation result in multiple newly formed voxel layers in the micro-CT image (Fig. 1L). As formation voxels can be associated with varying numbers of mechanical values (Table 1), mechanoregulation can no longer be accurately cap-


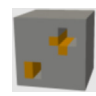
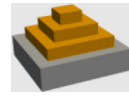
tured by the surface-based method due to shifting weight of the mechanical value in the analysis.

2.2. Volumetric mechanoregulation analysis

The volumetric mechanoregulation analysis was based on a (re)modeling image (Fig. 1A, 1B) clustered into formation volume, quiescent volume and resorption volume and the corresponding image of local tissue mechanical environment. The number of bins for the resulting histograms was specified dependent on the application like in the surface-based analysis (*in vivo*=50, *in vitro*=100).

Similar as in the surface-based method, the challenge was to associate formation with the underlying mechanical environment. Since the mechanical environment is calculated with the baseline image, there is no tissue in the formation volume yet (see Fig. 1D, E and G,H). Instead of using the formation-adjacent surface values, we projected the mechanical values at the surface onto the (yet empty) formation volume (see Fig. 1E), so that every formation voxel was associated with the mechanical value of the closest connected surface voxel. This way, the considered number of mechanical values in the mechanical image was exactly the same as the number of volume elements classified as formation in the

Table 1
Comparing the number of formation-associated mechanical values with the actual amount of formation voxels (ground truth) for the volumetric and the surface-based method.

Comparison amount of formation-associated values with ground truth						
	Flat surface		Concave surface		Multiple layers	
Ground Truth	9		32		56	
Volumetric Method	9		32		56	
Surface-Based Method	9		72		36	

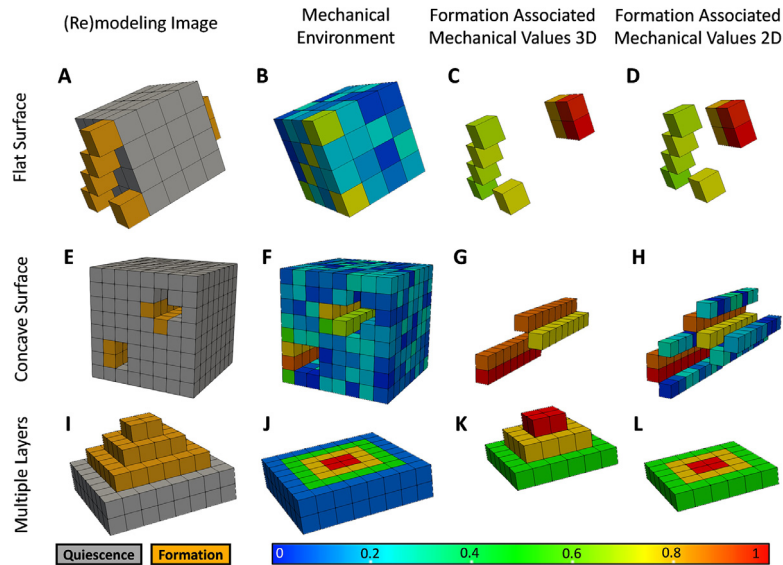


Fig. 2. Synthetic images: (A–D): Flat Surface, (E–H): Concave Surface, (I–L): Multiple layers. (A, E, I): (Re)modeling images with quiescence (grey) and formation (orange), (B,F,J): Mechanical environment on the quiescent surface, (C,G,K): Mechanical values (e.g. effective strain) associated with formation by the volumetric method, (D,H,L): Mechanical values associated with formation by the surface-based method.

(re)modeling image. We started with the mechanical data as input, which should have corresponding mechanical values for both the quiescent and the resorption volume, however not for the formation volume. To associate the underlying mechanical values at the surface with the formation volumes, we iteratively projected out the mechanical values on the surface layer by layer into the formation volume (see Fig. 1C, E).

First, we used a grey dilation (square connectivity =1, iteration=1) on the mechanical data, which is a mathematical morphology operation that projects the value in the center onto its 6 direct neighbors in the x, y, and z direction. In case of multiple adjacent values, it uses the maximum (Fig. 1Ei, E iv, K). Secondly, we calculated the difference between a binary dilation of the mechanical environment and the binarized mechanical environment, creating a mask of the next layer of voxels outside the surface. Third, we multiplied this layer with the formation volume and obtained a mask for the next layer of formation voxels. Lastly, we used this mask on the grey dilated mechanical values (Fig. 1Eii), and added this new layer of projected mechanical values to the original mechanical environment (Fig. 1Eiii). This then served as the start mechanical values of the next iteration.

The projection iterated through all formation layers (Fig. 1C), starting with the first layer (adjacent to the surface) and ending with the last layer (furthest layer from the surface), having filled all formation voxels from the (re)modeling image with values during the process (Fig. 1D, Ev). Using this layer-by-layer projection with the described kernel combined with the mask of the formation volume instead of a single-step projection with a large kernel allowed each formation voxel to be filled by a projection of

the closest connected mechanical surface value, while not distorting the original mechanical values (Fig. 1N).

The formation and resorption associated mechanical values were simply obtained by using formation or resorption area as a mask for the mechanical environment obtained by the iterative layer-by-layer projection (Fig. 1F,K). To get all mechanical values at the tissue surface, we created a mask for the tissue surface by subtracting a binary eroded image from a binarized image containing resorption and quiescence. The resulting surface mask image was then applied to the output mechanical signal image. For the quiescent surface, we used the mask for the tissue surface and excluded all surface voxels classified as resorption or projected onto formation areas. We used a grey dilation of the projected formation values and subtracted this from our original mechanical environment. Wherever on the tissue surface this subtraction resulted in a value of zero, this surface voxel was excluded from the mask used for the quiescent surface (Fig. 1F,K).

2.3. Synthetic data

We used three synthetic images to show the working principle of the volumetric method and illustrate the differences to the surface-based method. As an example of intrinsically flat surfaces, as often seen in trabecular bone, we created an image with a flat surface and single layer thick formation (Fig. 2A). Additionally, we created an example of formation within a concave surface (Fig. 2E), where formation voxels have multiple adjacent surface voxels, and an example of multiple voxel layers of formation on a flat surface (Fig. 2I). Corresponding images to represent the mechanical envi-

ronment on the surface were created by manually assigning values between 0 and 1 (Fig. 2B,F,J), to demonstrate the working principle of how to assess mechanoregulation in bone formation of both methods.

The number of formation voxels in the (re)modeling image (ground truth) was compared to the number of associated mechanical values (e.g. effective strain) by the volumetric and the surface-based method (Fig. 2C,D,G,H,K,L, Table 1). While the volumetric and the surface-based method included the same number of voxels on a flat surface (Fig. 2C,D; Table 1), the surface based method associated a larger number of mechanical values with formation on a concave surface (Fig. 2G,H; Table 1), and a lower number of mechanical values in case of multiple voxel layers of formation (Fig. 2K,L; Table 1).

Additionally to the numerical comparison, the results for the volumetric method (Fig. 2C,G,K) were visually compared to the mechanical environment on the surface (Fig. 2B,F,J).

2.4. In vitro data

For the *in vitro* data we used micro-CT images (36 μm voxel size) from hMSC cell-seeded hydroxyapatite (HA) polymer nanocomposite scaffolds, that were acquired weekly over a culture duration of 8 weeks from a previously published study by Schädli et al. [13] (detailed information in supplementary material 1.1). During the first 4 weeks, cell seeded scaffolds were cultured in standard growth cell culture medium, before switching to osteogenic cell culture medium in week 5. One group was subjected to cyclic mechanical loading while the other group served as a static control.

Obtained micro-CT images were registered [38], Gauss filtered (sigma 1.2, support 1) and binarized using a threshold of 138 mg/cm^3 HA (max. densities of the mineralized tissue at day 56: control: 289; loaded: 420 mg/cm^3 HA). The threshold was manually chosen such that after segmentation of the first week images, the average porosity was 83 % as reported by Schädli et al. [13]. (Re)modeling images were created by overlaying two subsequent time-lapsed images, clustering formation volumes where the second image showed mineral and the first did not, and quiescent volumes, where both images showed mineral (supplementary Figure S1). For the FE meshes, voxels were converted to 8 node hexahedral elements. Due to the range of tissue densities in the micro-CT images and the strong influence of it on the material properties [21] we chose to use heterogeneous material properties for the FE analysis. To consider the different material properties of scaffold and tissue, we used the binarized micro-CT image of the first time-lapsed scan (day07) as an approximation of the scaffold structure (supplementary Figure S1). A Young's modulus of 15 MPa was assigned to the original scaffold structure, corresponding to the value reported by Schädli et al. [13]. Voxels inside the binarized image but outside the day07 mask were converted to Young's modulus using the conversion function based on density published by Zhang et al. for *in vitro* tissue [21], instead of conversion functions for bone that are usually based on higher densities: $E = 62.53 * 10^6 * \rho^{7.4} + 3$, where E is Young's modulus in kPa and ρ is density in $\text{g HA}/\text{cm}^3$. A cylindrical mask of 6 mm diameter was fitted to the scaffold [13] and voxels inside this mask and outside the binarized image were assigned a Young's modulus of 2 kPa to account for structures of the scaffold that were segmented out due to the low image resolution but still affect the effective strain distribution during mechanical stimulation. The ratio between 2 kPa and 15 MPa is similar as used for bone and bone marrow in mice (see section 2.5). The Poisson's ratio was set to 0.3 for all values, according to previous work [21]. Due to the uneven top surface of the bone scaffolds, a padding was approximated at the top of the scaffold using a Young's Modulus of 5 GPa (material

stiffness of the piston during loading), to enable a larger contact area and more realistic force flow similar to modelling the intervertebral disks for *in vivo* FE-analyses [39,40].

2.5. In vivo data

For the *in vivo* analysis we used vertebral micro-CT images (10.5 μm voxel size) from mice, which were subjected to different compressive loading protocols: cyclic with 10 Hz, 5 Hz or 2 Hz, static or sham (0 N, control group). Following the 3R principles, we used this data from a previously published study by Scheuren et al. [6] (detailed information in the supplementary material 1.2). There were no statistical differences between time intervals in bone volume per total volume, trabecular thickness or number, or net remodeling rate and only mineralizing surface was higher in week 16–17 than in the other time intervals ([6], Figs. 1, 2). It was thus decided to use this time interval for the analysis. Grayscale micro-CT images were registered [38], Gauss filtered (sigma 1.2, support 1) and binarized using a threshold of 580 mg/cm^3 HA [6,41] and trabecular regions were automatically contoured. Segmented images were overlaid to create (re)modeling images clustered into formation volumes, where the week 17 image showed bone, but week 16 did not, resorption volumes, where the week 16 image showed bone but week 17 did not, and quiescent volume, where both images showed bone (supplementary Figure S1).

Leading up to the finite-element (FE) analysis, homogeneous material properties were assigned to the *in vivo* images, as previous studies have shown these to be effective [41,42]. A Young's modulus of 14.8 GPa and a Poisson's ratio of 0.3 was assigned to the binarized bone images, while the bone marrow within the bone cavity was assigned a Young's modulus of 2 MPa and a Poisson's ratio of 0.3 [39,41,42]. To ensure a more realistic force flow and to prevent unreasonably high strains on some nodes, intervertebral discs were added to proximal and distal ends of the vertebra [42]. For numerical reasons and since the parameters have marginal influence on the strain distribution in the bone [41], the same parameters as assigned to bone were used. Voxels were converted to 8 node hexahedral elements for the FE meshes.

2.6. Micro-finite element analysis

As described elsewhere [39], a 1% displacement of the length in the z-axis was applied to the top nodes, while the bottom nodes at $z = 0$ were constrained in all directions. Models averaged 20 million elements for the mouse vertebrae, and 2.2 million elements for the bone scaffolds. Micro-FE analysis was computed using the linear solver ParOsol [43] with one node and 12 cores, converging in 20 min for the mice vertebra and under 2 min for the bone scaffolds. Similar to Schulte et al. [4] and Scheuren et al. [6] we used strain energy density (SED) as mechanical signal for bone (re)modeling for the mouse vertebra. As the *in vitro* data was assigned heterogeneous material parameters in a large range, effective strain $\epsilon_{eff} = \sqrt{2U/E}$, where U is SED and E is Young's modulus, [44] was more appropriate to use as the mechanical signal for the bone scaffolds [41]. To enable a comparison between individual animals and loading groups, the mechanical signal was normalized within each sample and measurement by maximal SED or effective strain, chosen at the 99th percentile of values present in the VOI for mouse vertebra to exclude unrealistically high values [4]. The data of the bone scaffolds was more skewed, (8.9 % of values above the 50th percentile compared to 17 % in the mouse vertebra) causing large fluctuations in the conditional probabilities for the top bins (high effective strains) and decreased accuracy for the lower range. Thus we adjusted the normalization to the 90th percentile, leaving 3.4 % of the values in the 10 highest bins, comparable to the *in vivo* data (3.7 %). FE analysis was performed on the week 16

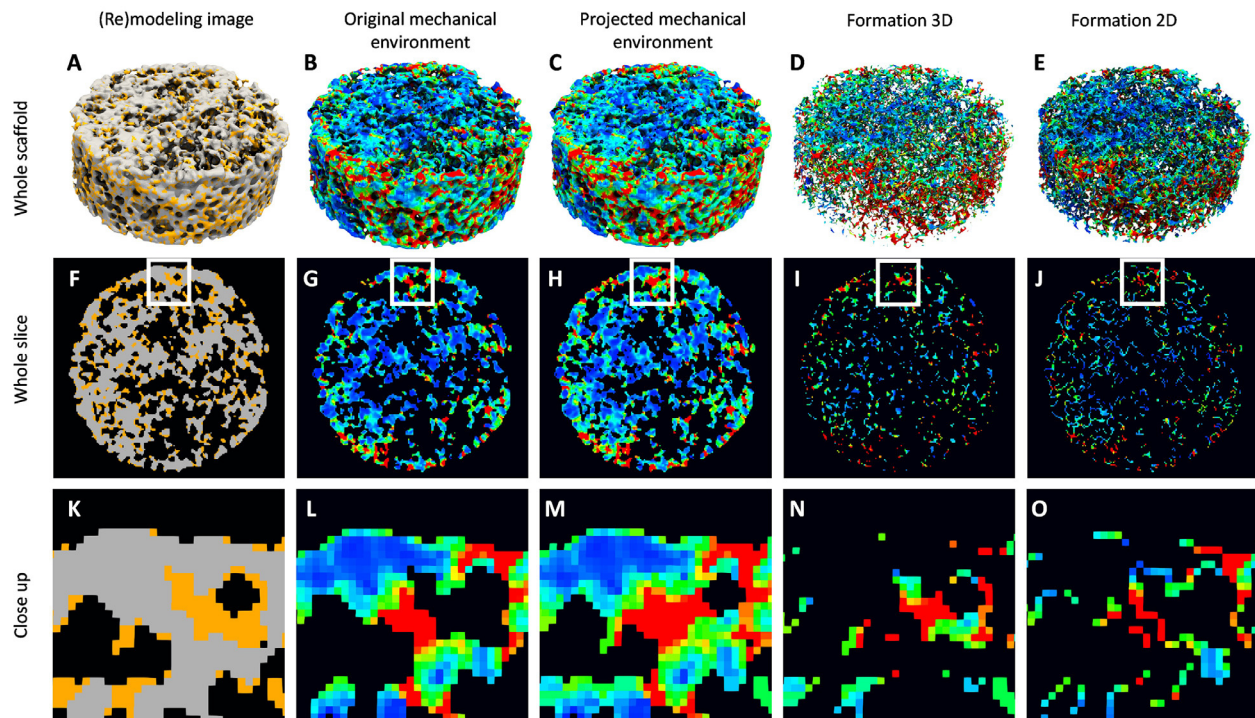


Fig. 3. Qualitative results and differences of applying the volumetric and surface-based method to a mechanically loaded scaffold. (Re)modeling image with formation (orange) and quiescence (grey) (A,F,K); original mechanical environment (FE results) corresponding to the quiescent data (B,G,L); projected mechanical environment (original mechanical environment and the projected formation values) (C,H,M); effective strain values associated with formation for the volumetric method (3D) (D,I,N), based on the original mechanical environment (B,G,L), which match the formation volumes displayed in (A,F,K); and surface-based (2D) method (E,J,O) corresponding to large parts of the surface; depicted in the whole 3D structure (A-E), single slice of the image (F-J), and a close up (K-O).

micro-CT image of the mouse vertebra, and on the images of week 1 to week 7 of the bone scaffold study.

2.7. Statistical analysis

Histograms were created based on the clustered mechanical values for formation, quiescence and resorption and input number of bins. Conditional probabilities were calculated as described in Schulte et al. [4], by first rescaling the histograms to amount to 1, normalizing all (re)modeling events to remove the dependence on the imbalance of formation and resorption, which may vary between different groups and animals. Second, the conditional probabilities were calculated bin-wise based on the adjusted histograms, dividing each histogram value by the sum of the histogram values of all (re)modeling events for this bin. Third, exponential functions as introduced by Schulte et al. [4] were fitted to the conditional probability curves by using a least square optimization. The correct classification rate (CCR) was calculated based on the conditional probabilities [5]. CCR is a quantitative measure to assess mechanoregulation resulting in a value between 0.33 or 0.5 (for 3 or 2 (re)modeling events respectively) and 1, with 1 meaning (re)modeling is completely controlled by the mechanical environment and 0.33 or 0.5 meaning (re)modeling is completely independent of the mechanical environment. Additionally, the area under the curve for the receiver operating curve (AUC) was calculated for each (re)modeling event, using the clustered mechanical values and the mechanical values at the surface [5,6]. Similarly to the CCR, AUC is a quantitative measure between 0.5 ((re)modeling event is independent of the mechanical environment) and 1 ((re)modeling is completely controlled by the mechanical environment) to assess mechanoregulation for each (re)modeling event. The mean SED and effective strain for each (re)modeling event was calculated from the clustered mechanical values using micro-FE analysis. Further-

more, we conducted a sensitivity analysis regarding lower image resolution for both methods (supplementary material 1.3, Figure S3).

The parameters of the fitted exponential curves were tested for normality and consequently for significance using unpaired student's *t*-test to compare results between groups and a paired student's *t*-test to compare results between methods. Results of CCR, AUC and mean SED or effective strain were first tested with Shapiro-Wilk test whether the data were normally distributed. When distribution was not normal, then we used Mann-Whitney U test or Wilcoxon when comparing intra-group differences. Otherwise, statistical analysis was performed by an unpaired student's *t*-test to compare results between groups and a paired student's *t*-test to compare results between methods. Benjamini-Hochberg correction was used to adjust for multiple comparisons.

3. Results

3.1. In vitro data

We analyzed mechanoregulation of bone formation in hydroxyapatite scaffolds seeded with human mesenchymal stem cells that were incubated over 8 weeks with one mechanically loaded and one control group from a study by Schädli et al. [13]. As the *in vitro* study only included the osteoblastic cell lineage, there was no resorption in this study. In week 1 there were air bubbles present in the scaffold structure [13], omitting a correct analysis, so that these results were moved to the Supplementary material (Figure S4). Fig. 3 shows the application and the differences of the volumetric and the surface-based method to a loaded scaffold on the whole 3D structure (Fig. 3A-E), a 2D slice (Fig. 3F-J) and a close up (Fig. 3K-O). A close up of the (re)modeling image (Fig. 3K), the original mechanical environment (Fig. 3L), and the projected

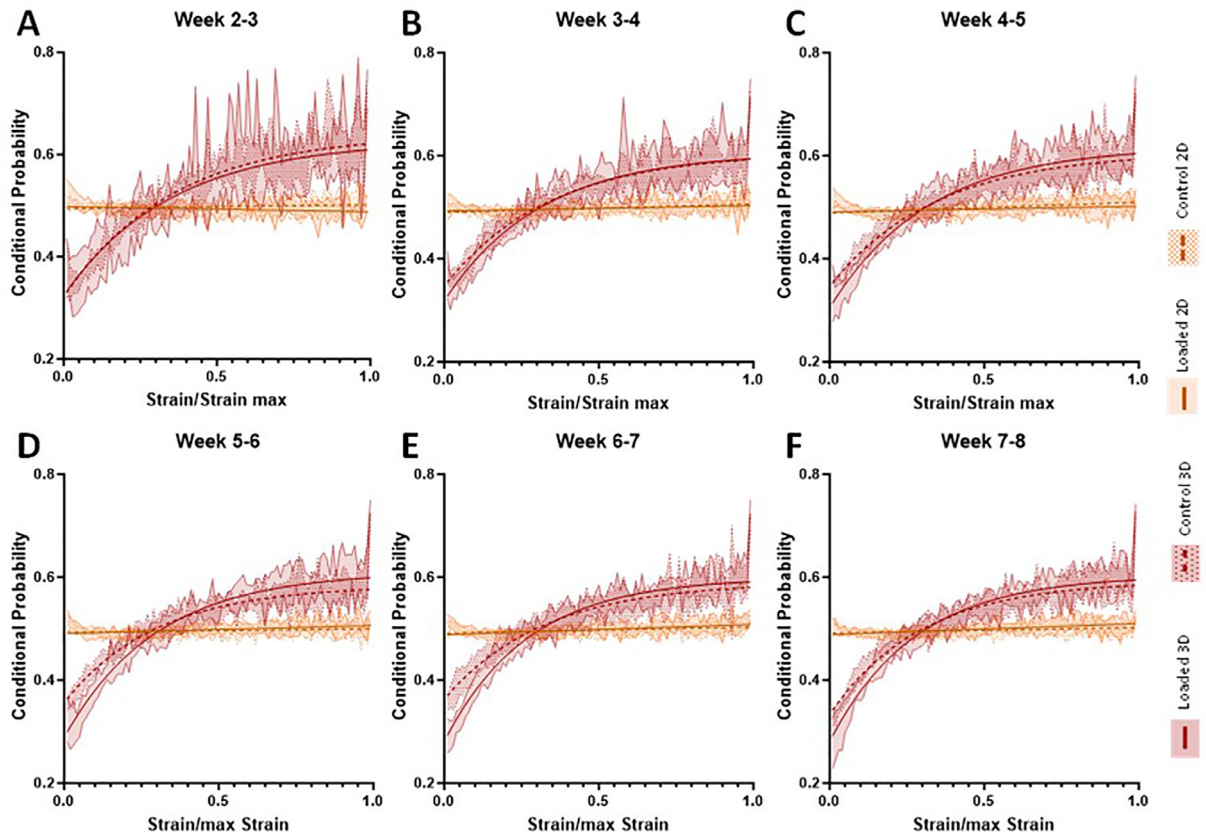


Fig. 4. Conditional probability curves for bone formation in time-lapsed *in vitro* data, comparing the volumetric (3D) and surface-based (2D) method for the loaded and control group. (A): Week 2–3. (B) Week 3–4. (C): Week 4–5. (D): Week 5–6. (E) Week 6–7. (F): Week 7–8. The 3D method detects mechanoregulation for bone formation for both loaded and control group (probability increases with increasing effective strain), while the 2D method fails to detect mechanoregulation.

mechanical environment are illustrated in Fig. 3M. Notably, the original mechanical environment was kept, so that the differences between the original and the projected mechanical environment was hardly visible on the whole slice (Fig. 3G,H) and the 3D image (Fig. 3B,C). When comparing the formation associated effective strain values from the volumetric and the surface-based method in the 3D images (Fig. 3D, E), the surface-based method included a higher number of values, namely most of the scaffold's surface. The whole slice (Fig. 3I, J) and the close up (Fig. 3N, O) of the associated formation show that the volumetric method seemed to include more localized values in the actual formation areas. This resulted in more values being included in the surface-based method on uneven surfaces with little formation, but less values included in areas with high effective strain and a large amount of formation (Fig. 3N, O). Overall, the close ups in Fig. 3K and L suggested, that the bone scaffolds are mechanoregulated, as there were larger amounts of formation in areas with high effective strain, as well as less formation in areas with low effective strain. To visualize this process, we calculated the conditional probabilities for formation for each week, group, and method (Fig. 4) which showed the conditional probability of formation occurring at a given local surface strain. As there was only formation and quiescence in terms of (re)modeling events, the corresponding quiescent curve was simply the inverse of the depicted curves and was thus not displayed. The parameters from the fitted exponential function are displayed in Table 2.

The volumetric method shows mechanoregulation over all time points for both groups, loaded and control, where the probability for formation increased with increasing effective strain. However, the surface-based method failed to detect mechanoregulation, as it indicated only non-targeted formation for both the loaded and

control group, with a constant probability around 0.5. In the week 2–3 (Fig. 4A) and 3–4 (Fig. 4B), the probabilities calculated with the volumetric method were similar in the control group and the loaded group. After week 4 (Fig. 4C–F), the control curve started at a higher and ended at a lower probability than the loaded counterpart, indicating that the loaded group was more mechanoregulated than the control group. Especially in week 5–6 (Fig. 4D) and week 6–7 (Fig. 4E), the higher probability of the control curve compared to the loaded curve below 0.3 strain/max strain was clearly visible. Towards the later time points of the study, the standard deviation decreased, especially for the results obtained with the volumetric method. Fitting an exponential function to the average data calculated by the surface-based method resulted in all but one R^2 value being below 0.5 (Table 2).

For the surface-based method, the parameter a stayed constant throughout the time of the study and for both groups ($a = 1.000$). However, in this case, a can arguably not be interpreted as a measure for mechano-sensitivity. The indicator of the amount of non-targeted formation, parameter y_0 , stayed very similar throughout the time in the control group (a ranging from 0.4888 to 0.4938), while it decreased very slightly over time in the loaded group (from $a = 0.4981$ to $a = 0.4883$). However, there were no differences ($p > 0.05$) between parameters obtained for the loaded and the control group after assessment with the surface-based method.

While the amount of non-targeted formation, parameter y_0 , did not follow a trend for the control group when analyzed with the volumetric method, the loading group showed a decrease over time (from $y_0=0.3237$ to $y_0=0.2806$). Overall, the values of parameter y_0 were significantly higher for the control group compared to the loaded group ($p < 0.01$). In addition, the values for the parameter a were significantly lower for the control group than the

Table 2
Parameters for fitted exponential functions to the conditional probability for formation for both volumetric and surface-based method, loaded and control group.

Volumetric			Wk 2–3	Wk 3–4	Wk 4–5	Wk 5–6	Wk 6–7	Wk 7–8
Control	y_0		0.3214	0.3468	0.3459	0.3563	0.3630	0.3331
	a		0.3191	0.2596	0.2611	0.2279	0.2276	0.2598
	b		2.7514	2.8969	2.8584	3.2989	3.0388	3.3278
	R ²		0.9511	0.9703	0.9756	0.9641	0.9619	0.9675
Loaded	y_0		0.3237	0.3181	0.3043	0.2888	0.2808	0.2806
	a		0.3034	0.2879	0.3137	0.3216	0.3186	0.3231
	b		2.7820	3.1342	3.0703	3.2934	3.6238	3.5424
	R ²		0.9101	0.9654	0.9828	0.9834	0.9800	0.9841
Surface-Based			Wk 2–3	Wk 3–4	Wk 4–5	Wk 5–6	Wk 6–7	Wk 7–8
Control	y_0		0.4938	0.4899	0.4888	0.4923	0.4913	0.4912
	a		1.0000	1.0000	1.0000	1.0000	1.0000	1.0000
	b		0.0080	0.0161	0.0206	0.0074	0.0117	0.0107
	R ²		0.1225	0.3023	0.4241	0.0736	0.1960	0.1844
Loaded	y_0		0.4981	0.4926	0.4906	0.4907	0.4883	0.4887
	a		1.0000	1.0000	1.0000	1.0000	1.0000	1.0000
	b		−0.0099	0.0101	0.0111	0.0153	0.0198	0.0210
	R ²		0.1090	0.1322	0.1272	0.3011	0.4550	0.5229

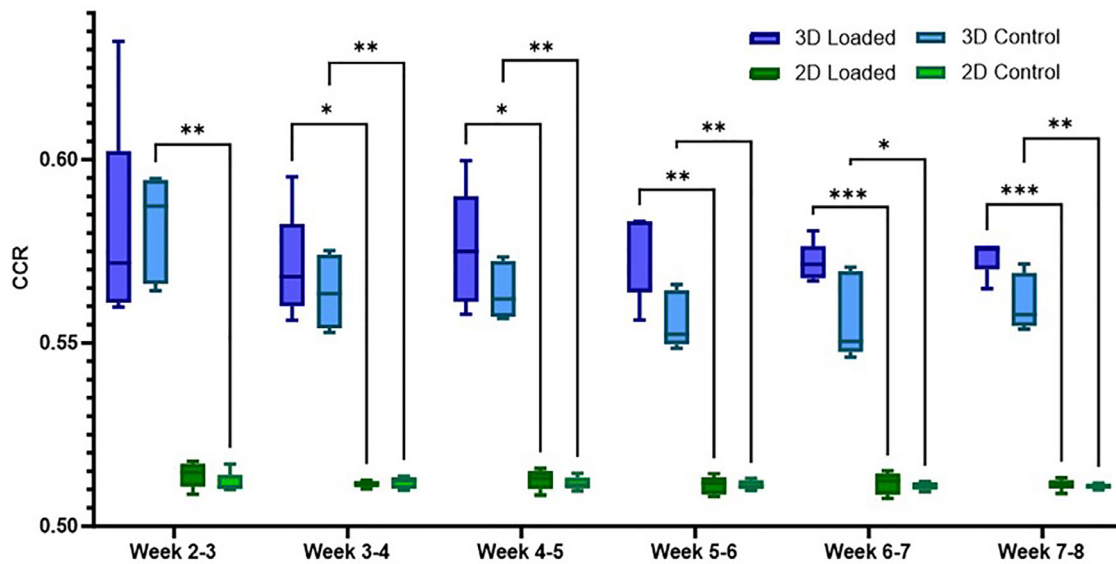


Fig. 5. Correct Classification rate (CCR) over the duration of the *in vitro* study, showing significantly higher results for the 3D method compared to the 2D method, however no group differences. * $p < 0.05$; ** $p < 0.01$; *** $p < 0.001$.

loaded group ($p < 0.05$). To quantify the mechanoregulation visible in the probability plots, we calculated the CCR value (Fig. 5), and the AUC_{formation} (Fig. 6).

After week 3, the loaded and control groups exhibited significantly higher CCR values when using the volumetric assessment compared to the surface approach (Fig. 5). At week 2–3, the CCR value for the control group was significantly higher for the volumetric than for the surface-based method. While the CCR values for the loaded group were slightly higher than those of the control group after week 3, there are no significant differences between the groups when calculated with the volumetric method. The CCR values calculated by the surface-based method are close to 0.5, which would imply non-targeted bone formation. There are no differences between groups using the surface-based method (Fig. 5).

Fig. 6 shows that the resulting AUC values are significantly higher when calculated with the volumetric method compared to the surface-based for both the loaded and the control group. With values above 0.6, the results indicate mechanoregulation in both the loaded and the control group. After week 5, the AUC value for

the loaded group was significantly higher than that of the control group, when calculated with the volumetric method ($p < 0.05$). After week 6, the standard deviation of the AUC values in the loaded group drastically reduced while there was no change in the control group. However, when using the surface-based method, there are no significant differences between the loaded and the control group and all values are only slightly above 0.5, which implies non-targeted bone formation instead of mechanoregulation in the bone scaffolds.

3.2. In vivo data

In the second part of our study, we investigated the applicability of the volumetric method to *in vivo* data. The surface-based method took on average 3.52 s to compute, compared to 37.3 s for the more complex volumetric method. Fig. 7 shows a qualitative visualization of mechanoregulation and the differences between the volumetric (3D) and the surface-based method (2D). Fig. 7K, L and M illustrate a qualitative example of mechanoregulation with

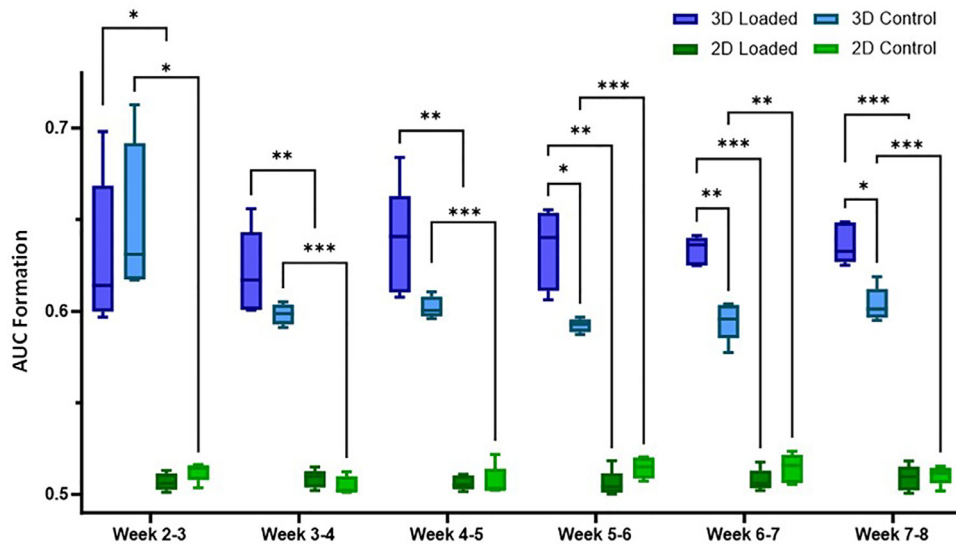


Fig. 6. Area under the curve for the receiver operating curve (AUC) for formation over the duration of the *in vitro* study, showing significantly higher values for the loaded group compared to the control group after week 5 when applying the volumetric method. * $p < 0.05$; ** $p < 0.01$; *** $p < 0.001$.

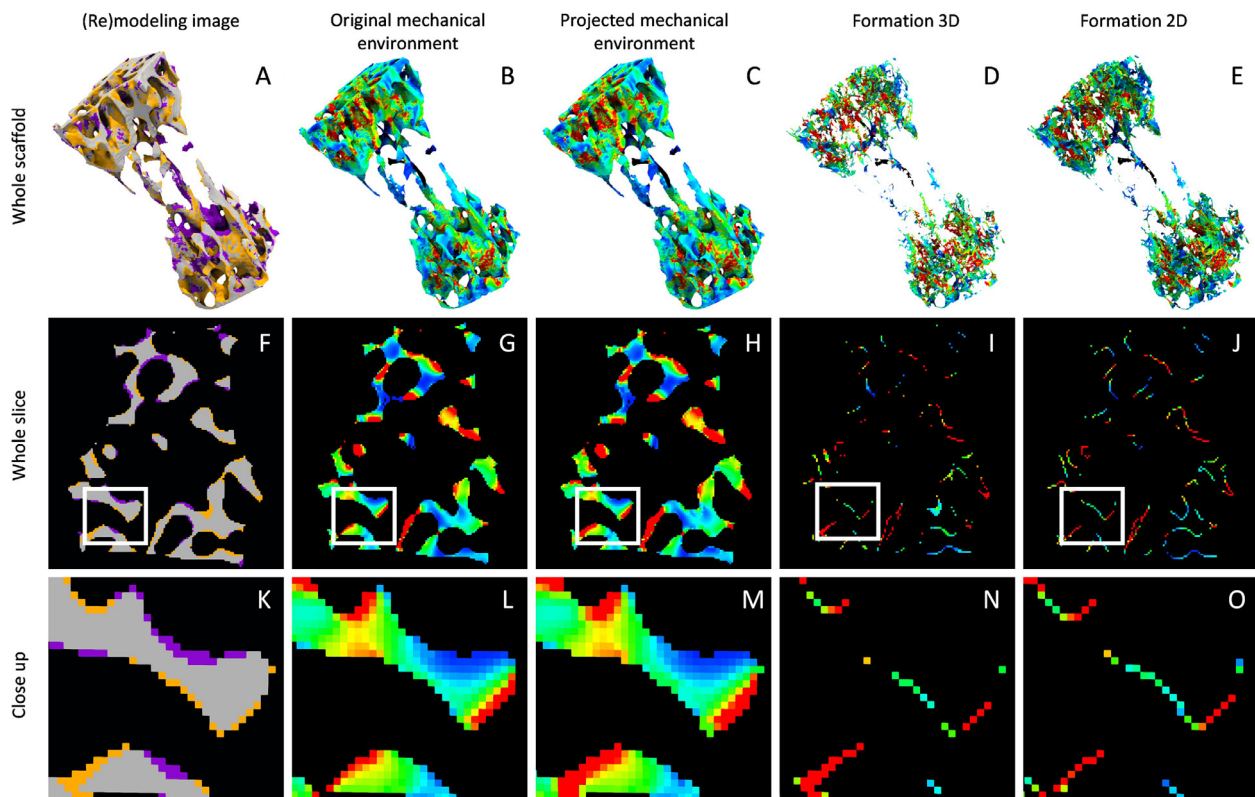


Fig. 7. Qualitative visualization of mechanoregulation and the differences between the volumetric and the surface-based method (example of 2 Hz group): (Re)modeling image (A,F,K), original mechanical environment (FE results) (B,G,L), projected mechanical environment: original mechanical environment and the projected formation values (C,H,M); SED values associated with formation for the volumetric (3D) (D,I,N) and surface-based (2D) method (E,J,O); depicted in the whole 3D structure (A–E), single slice of the image (F–J), and a close up (K–O). The formation associated mechanical values calculated by the 3D method (D,I,N) correspond directly to the formation volumes (A,F,K), while the 2D method includes more surface values, leading to small differences between the methods.

formation in areas of high SED and resorption in areas with low SED, which was captured by both the surface-based and volumetric method (Fig. 7N, O). The differences between the methodology of the surface-based and the volumetric mechanoregulation method are clearly visible in the 3D images of the associated formation (Fig. 7D,E). The surface-based results resemble the trabecular surface, while the volumetric results look like localized components consistent with the depicted bone formation (Fig. 7A). Nevertheless, the formation associated mechanical values and the amount

thereof hardly changed, visible from the images of the whole slice (Fig. 7I,J). Small differences can be observed in the lower left corner of the close-ups (Fig. 7N,O), where the volumetric method includes more high values than the surface-based, and the middle of the close-ups, where the surface-based method includes more medium values than the volumetric method.

Fig. 7 panels B, C, G, H, L, M show that the original mechanical values from the FE analysis are kept for the quiescent and resorption volumes. The mechanical values at the surface are projected

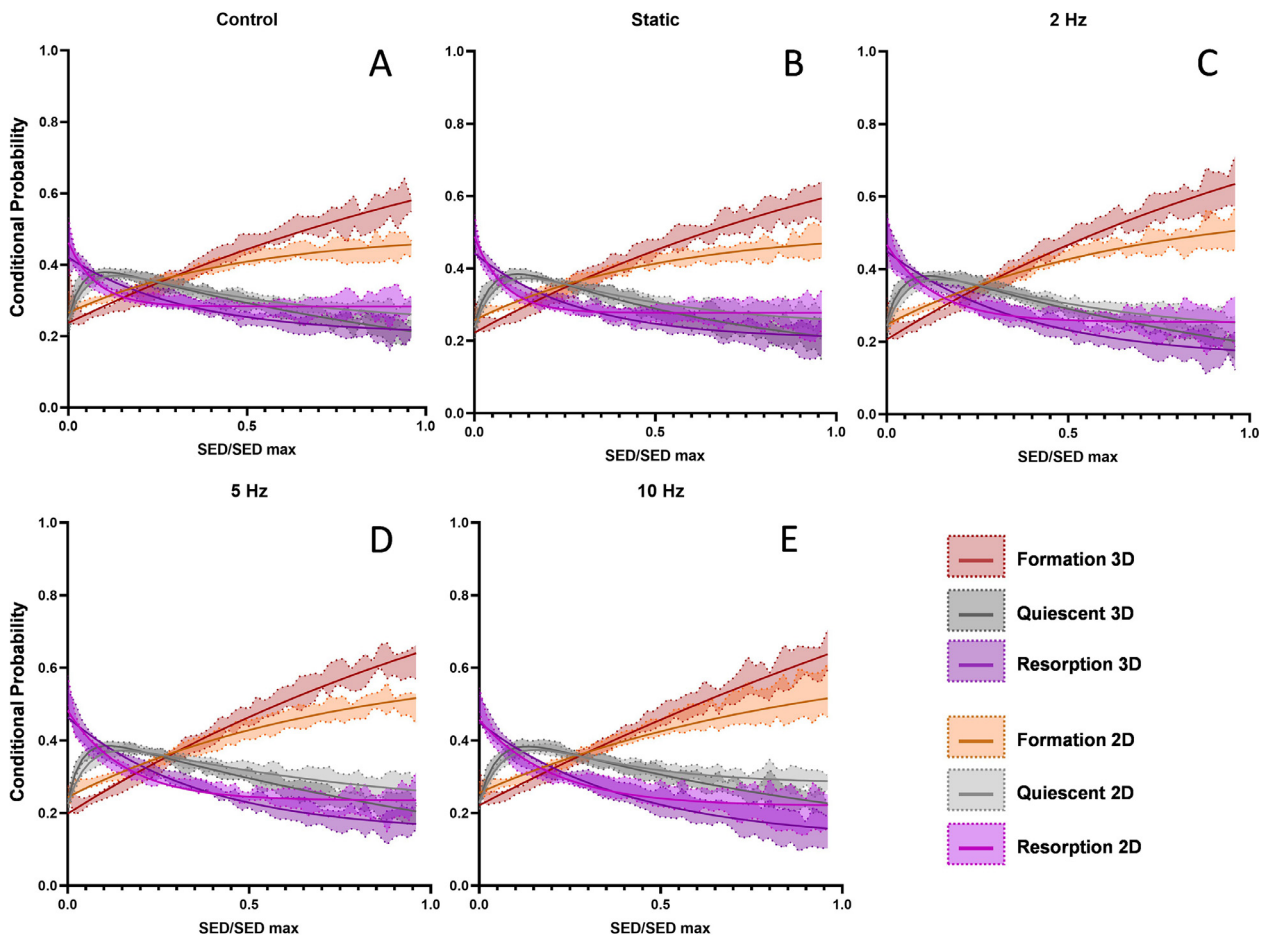


Fig. 8. Conditional Probability Curves for Control, Static, 2 Hz, 5 Hz and 10 Hz group, showing resorption, quiescent and formation for both the surface-based (2D) and volumetric (3D) method, depicted as standard deviation areas and the fitted exponential function to the average values. Probability curves from both methods show mechanoregulation, with the 3D method resulting in a steeper formation probability curve with a larger increase compared to the 2D method, indicating higher mechanoregulation could be detected by the 3D method.

onto the formation volumes, demonstrating that the algorithm predicts formation even in an *in vivo* situation.

Mechanoregulation was visualized by conditional probability plots (Fig. 8) that show the likelihood of a formation or resorption event at given SED. The plots illustrate the exponential function fitted to the average values and the standard deviation depicting the conditional probabilities for formation, quiescent and resorption for both the volumetric and the surface-based method. The parameters corresponding to the fitted exponential curves are listed in Table 1. The formation curve for the volumetric method generally starts at a lower probability at 0 SED/SED_{max} and reaches a higher probability at 1 SED/SED_{max} than the surface-based method. As shown in Table 1, 2 Hz and 5 Hz groups show the lowest non-targeted formation, which is represented by parameter y_0 (2 Hz: $y_0=0.206$ (3D), $y_0=0.247$ (2D); 5Hz: $y_0=0.198$ (3D), $y_0=0.206$ (2D)).

The slopes of the formation curves, which can be interpreted as an indicator of mechano-sensitivity and are described by the parameter a (Table 3) were consistently higher for the volumetric method compared to the surface-based method. The highest mechano-sensitivity values (3D: $a = 1.341$, 2D: $a = 0.396$) were obtained with 10 Hz loading. The volumetric method resulted in a highest maximum probability of 0.640 at 5 Hz (Fig. 8D) and the lowest 0.580 was found in the control group (Fig. 8A). Similarly, the surface-based method resulted in a highest maximum probability of 0.516 at 5 Hz (Fig. 8D) and the lowest 0.457 for control (Fig. 8A). This means that the volumetric method resulted in an increase of 24 % - 27 % compared to the surface-based method re-

spectively. The 10 Hz data (Fig. 3D) notably had the highest standard deviation for both methods. The exponential functions fitted similarly well to the average data for both methods, with an overall R^2 of 0.983 ± 0.006 (3D) and 0.985 ± 0.006 (2D) across all groups.

Quiescent curves show similar behavior between the surface-based and volumetric method below 0.4 SED/SED_{max}, however the volumetric method results in lower probabilities above that value. For both methods, there were no notable differences between groups in the quiescent probability curves, in contrast to the formation and the resorption curves.

The resulting resorption curves from the surface-based method start with a steep decline ($b = 4.744-12.161$) below 0.1 SED/SED_{max} and then plateau above 0.5 SED/SED_{max} (Fig. 8). The resorption curves from the volumetric method start at a lower probability and with less steep slope ($b = 2.343-3.378$) compared to the surface-based method but continue to decrease above 0.5 SED/SED_{max} instead of reaching an asymptotic value. For both the volumetric and the surface-based method, the 10 Hz group had the lowest non-targeted resorption with $y_0=0.125$ and $y_0=0.219$ respectively. While resorption is less than or equally probable as quiescence at above 0.9 SED/SED_{max} for the control and the static group, it becomes increasingly less probable in the groups that were cyclically loaded. Overall, the conditional probability curves from the volumetric method are steeper above 0.4 SED/SED_{max} than those of the surface-based method, which indicates that mechanoregulation is still sensitive to an increase of SED above that level, in contrast to the narrower curves from

Table 3
Parameters of the fitted exponential functions for the conditional probability curves *in vivo*.

Parameters	Volumetric / 3D					Surface-based / 2D					
	Control	Static	2Hz	5Hz	10Hz	Control	Static	2Hz	5Hz	10Hz	
Formation	y_0	0.2372	0.2223	0.2058	0.1983	0.2212	0.2655	0.2571	0.2472	0.2437	0.2555
	a	0.7146	0.7037	0.8434	0.9120	1.3413	0.2201	0.2482	0.3333	0.3735	0.3959
	b	0.6681	0.7659	0.7260	0.6765	0.3790	2.0689	1.9498	1.5236	1.3388	1.0956
	R^2	0.9704	0.9871	0.9838	0.9872	0.9864	0.9744	0.9874	0.9849	0.9885	0.9915
Resorption	y_0	0.2056	0.2049	0.1529	0.1463	0.1247	0.2831	0.2771	0.2542	0.2345	0.2192
	a	0.2152	0.2372	0.2966	0.3174	0.3250	0.1790	0.2106	0.2131	0.2475	0.2375
	b	2.9379	3.3782	2.5860	2.6497	2.3435	12.156	12.161	7.2012	6.1932	4.7440
	R^2	0.9832	0.9717	0.9916	0.9800	0.9795	0.9422	0.9669	0.9579	0.9430	0.9406

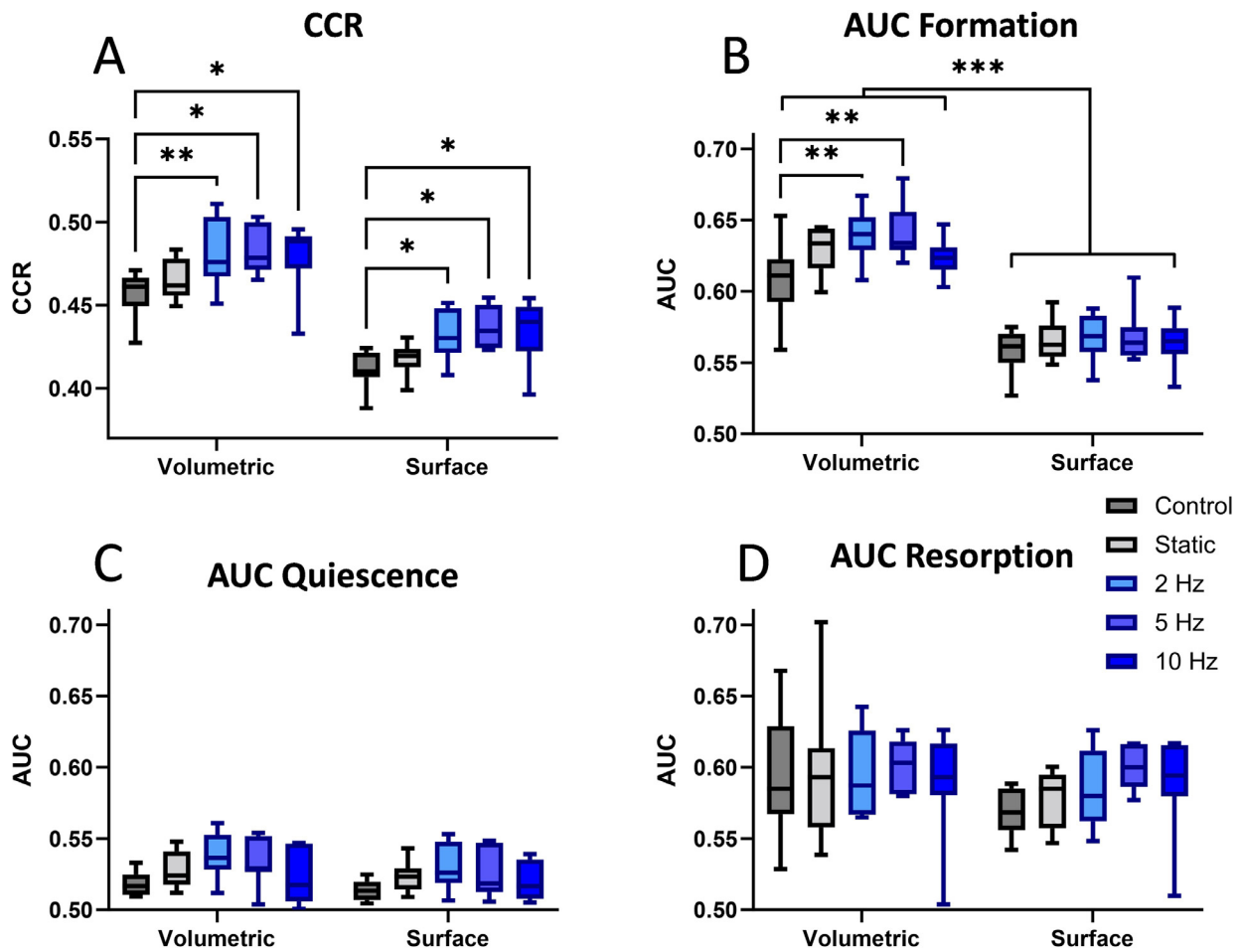


Fig. 9. Quantification of mechanoregulation for *in vivo* data. (A): Correct classification rate (CCR) for *in vivo* data. (B–D): Area under the curve of the receiver operating characteristic (AUC) for formation (B), quiescent (C) and resorption (D). Both methods detected cyclic loading resulting in increased overall mechanoregulation (CCR) compared to control group, while increased mechanoregulation of formation (AUC) was detected for 2 Hz and 5 Hz only using the 3D method compared to control. * $p < 0.05$; ** $p < 0.01$; *** $p < 0.001$.

the surface-based method. The exponential functions fit for the 3D method was $R^2=0.981\pm0.006$ compared to $R^2=0.950\pm0.01$ for the 2D method, meaning the results obtained with the volumetric method still follow the proposed functions suggested by Schulte et al. [4].

To statistically analyze and quantify the differences visible in the conditional probability plots, CCR and AUC for formation, quiescent and resorption were calculated (Fig. 9). CCR values for the 2 Hz, 5 Hz and 10 Hz group were significantly higher than for the control group ($p < 0.05$) for both methods (Fig. 4A). CCR values for the volumetric method are significantly higher (10–11 %) than those from the surface-based method ($p < 0.0001$).

While there are no differences between the $AUC_{\text{formation}}$ values for all groups from the surface-based method, both 2 Hz and 5 Hz groups show significantly higher ($p < 0.01$) values than the control group when calculated with the volumetric method (Fig. 9B). AUC values for formation were also significantly higher (9–13 %) for each group when calculated with the volumetric method compared to the surface-based result ($p < 0.001$).

We found no differences between groups and methods for $AUC_{\text{quiescent}}$ values (Fig. 9C). There were also no differences between groups and methods for the $AUC_{\text{resorption}}$ values, however the standard deviation for both the static and control group were notably higher for the volumetric method (Fig. 9D). The results for

the resolution sensitivity analysis can be found in the supplementary material 1.3 and Figure S3.

4. Discussion

In this study, we have developed a volumetric method to quantify mechanoregulation of bone formation in tissue engineering applications based on time lapsed micro-CT images and FE analysis. We were able to quantify mechanoregulation in mechanically loaded and unloaded *in vitro* tissue engineered bone constructs. Additionally, mechanoregulation measured by $AUC_{\text{formation}}$ was significantly higher for loaded samples than in the control group from week 5 on. The surface-based method did not detect any mechanoregulation. We showed that the volumetric method is suitable to analyze mechanoregulation in *in vitro* tissue engineered bone constructs.

After 5 weeks of culture, loaded samples showed significantly higher $AUC_{\text{formation}}$ and thus higher mechanoregulation of tissue formation than the control group. Notably, this time-point aligns with the timing in the original study, where osteogenic medium was introduced to the culture [13]. This enabled osteoblast differentiation into osteocytes, so that the differences could be due to the mechano-sensing of the osteocytes and their communication with the osteoblasts [45]. Yet our results show that osteoblasts alone are also affected by mechanoregulation, similar as in billfish bones that are mechanoregulated despite not having osteocytes [46]. However, osteocytes seem to make this process more sensitive and amplify it, as also indicated by the decrease in the non-targeted formation (parameter y_0) in the loaded group after week 5. Our results are in line with earlier studies that showed mechanoregulation in particular small subregions bone scaffolds [32] and 2D osteoblast cultures [31] as well as studies that showed increased mineralization due to mechanical loading [13,21,28]. The values we found for $AUC_{\text{formation}}$ are in a similar range as the evaluated *in vivo* data [6] and values reported in fracture healing in mice [5,47].

Interestingly, we found mechanoregulation *in vitro* not only for the loaded, but also the control group according to CCR and $AUC_{\text{formation}}$. However, we see similar results *in vivo*, where no superphysiological application of mechanical stimulation still leads to mechanoregulation, even in not load-bearing bones [6,48]. Liu et al. showed that *in vitro*, hydrostatic load can already induce osteodifferentiation [49], while Sittichokechaiwut et al. and Brunelli et al. include resting periods of 5 days or more between loading cycles [29,50], making it seem likely that already small mechanical impulses can cause mechanoregulation. Even the control samples experience gravity, movements during bioreactor handling and internal stress from fabrication and interaction with the culture media. Additionally, the control samples were cultured in the same bioreactors and medium as the loaded samples [13], so that they might have been affected by the mechanical loading of the other scaffold. Nevertheless, a more detailed analysis with using FE models for the mentioned alternative loading scenarios will be necessary to gain further insights into why exactly the control samples also exhibit mechanoregulation.

By including CCR as a statistical measurement of mechanoregulation, in the *in vivo* study both the surface-based and the volumetric method were able to show significant differences between the cyclically loaded groups (2 Hz, 5 Hz, 10 Hz) and the control group *in vivo*, meaning that cyclic loading increases mechanoregulation. When using the volumetric approach, we detected significantly higher $AUC_{\text{formation}}$ values for both the 2 Hz and the 5 Hz group compared with the control group. Both CCR and $AUC_{\text{formation}}$ values were significantly higher when calculated with the volumetric method compared to the surface-based method, indicating more targeted (re)modeling and especially formation than initially

reported. The results for $AUC_{\text{quiescent}}$ and $AUC_{\text{resorption}}$ were similar between methods and not significantly different between groups. Our results show that both the surface-based and the volumetric method can detect bone mechanoregulation and differences from different loading conditions in trabecular bone *in vivo*. The volumetric method was more sensitive to differences in mechanoregulation of bone formation, indicating the volumetric method should be especially considered when investigating differences between groups in bone formation.

We found increased mechanoregulation of bone formation for a loading frequency of 2 and 5 Hz *in vivo* (Fig. 9). However, the $AUC_{\text{formation}}$ value indicated a threshold frequency at 5 Hz, above which mechanoregulation in bone formation already decreased for a loading frequency of 10 Hz (Fig. 4B). Previous studies by Scheuren et al. [6] and Kameo et al. [51,52] reported that 10 Hz leads to the highest bone formation rate, above which an increase in frequency does not result in additional benefits for bone (re)modeling. However, our results suggest, that loading at 10 Hz already results in less mechano-sensitive (re)modeling than loading at 5 Hz. Warden and Turner [53] also reported the highest bone formation rate for a loading frequency of 10 Hz, but concluded an optimal loading frequency of 5–10 Hz, as the resulting mechanical properties were highest with a loading frequencies of 5 Hz. Tanaka et al. [54] found that a loading frequency of 2 Hz resulted in higher osteoblastic calcification compared to 10 Hz *in vitro*, while Lewis et al. [55] found the highest calcium response of osteocytes at a frequency of 1 Hz. These findings support our conclusion that cyclic loading with 2–5 Hz increases mechanoregulation in bone formation, and that although loading above 2–5 Hz increases bone formation in general, it also leads to more non-targeted formation.

While the volumetric method leads to different results for formation compared to the surface-based method, the results for quiescence and resorption are not significantly affected. As formation is projected onto the bone surfaces by the surface-based method, many additional surface values are included in concave structures such as scaffolds with typically high porosity [56]. Additionally, the surface-based method neglects the thickness of bone formation or depth of resorption [41], whereas the volumetric method also considers the thickness or depth of the (re)modeling events. While this increases the differences visible in the formation assessment, it does not change the results for resorption significantly, as the resorbed volumes are rather shallow. However, these increased results for mechanoregulation in bone formation could mean that we have previously underestimated the influence of mechanical environment on the (re)modeling process. This suggests that mechanical loading as in physical exercise should be paid more attention as a treatment option to improve bone strength, in line with a recent study that indicated high intensity exercise increases bone strength [57]. It does not only increase bone formation, but also ensures that this is more targeted, leading to an even larger benefit.

A limitation of the proposed algorithm is that it favors mechanoregulation due to choosing the maximum mechanical value for the projection when presented with multiple options during the grey dilation. However, this is based on the biological assumption, that osteocytes rather sense and communicate the highest effective strain than an average value [37]. Even though the 10 Hz group from the *in vivo* study resulted in the highest bone formation rate [6], it does not result in the highest $AUC_{\text{formation}}$ (Fig. 9), showing that the differences we found are not due to a bias in the method.

Another limitation of the method is that, while it is more sensitive to differences in mechanoregulation, it is also more sensitive to certain errors in the imaging and imaging preprocessing pipeline, which is visible in small spikes at very low SED for the conditional probability curves for formation (Fig. 8). These are the

result of particular trabeculae being erroneously segmented out and the resulting structures thus considered a ‘dead end’ in the FE leading to very low local SED. If these structures are less segmented out in the next time-point, a large volume will be labeled as formation and associated with the low SED values. This problem affects the volumetric method more than the surface-based method but does not largely affect the exponential curve fit. Our results of the sensitivity analysis (supplementary Figure S3) show that the volumetric method is less sensitive to image resolution than the surface-based method. However, a rigorous sensitivity analysis regarding all changed parameters in the *in vitro* study compared to the *in vivo* study has not been performed, presenting a limitation of this study.

Generally imaging is striving to always achieve higher imaging resolutions, where it will be more important to differentiate between the different thicknesses of formation and resorption. As this is comparable to our synthetic image showing multiple layers of formation (Fig. 11-L), the volumetric method would be more appropriate to fully leverage the information we gain from the higher resolution. Similarly, the volumetric method should also be considered when investigating studies with more bone formation, e.g. with anabolic treatments. When wanting to use a surface-based method, the higher resolution or higher formation activity could be counteracted by shorter time intervals between scanning, if possible.

Lastly, the *in vitro* study did not include resorption because its primary aim was to investigate the osteogenic potential for implantation. However, this can also be considered a strength, because the reduced complexity allowed us to focus solely on tissue formation. But as the CCR value is a measure of mechanoregulation across all (re)modeling events, those values are not comparable to *in vivo* results from the literature and it is likely the reason for missing significant differences between groups in the CCR values.

While mechanoregulation has been the subject of investigation in many studies both *in vivo* and *in vitro*, results have frequently been shown by comparison of bone formation under different conditions, or by the comparisons of mean strain in sub-regions [32,58,59]. Quantitative metrics to compare results cross studies are often lacking. In this study we used AUC and CCR to quantify the amount of mechanoregulation, which were first introduced by Tourolle et al. [5], and parameters obtained for the conditional probability curves [38]. These parameters provide insights into how much of the (re)modeling process is targeted or non-targeted [60–62]. The CCR provides one metric with high statistical power regarding the mechanoregulation of all (re)modeling events [63] as used by Marques et al. [41]. However, AUCs can be valuable to gain specific information about mechanoregulation in formation or resorption. This includes studies that only investigate formation such as many *in vitro* studies [13,21,64]. The AUC can quantify the amount of targeted and non-targeted (re)modeling for formation or resorption specifically and enables statistical comparisons between multiple groups or mechanical signals [6].

A different approach of analyzing mechanoregulation is deriving parameters based on Frost’s mechanostat theory [65], that (re)modeling velocity is dependent on mechanical signal. Marques et al. and Birkhold et al. have successfully used this concept to compare mechanoregulation between different groups by parametrizing the resulting curves [41,66]. However, the conventional approach neglects non-targeted (re)modeling and is not applicable to studies investigating only formation or resorption. A solution for this could be to derive two separate functions for formation and resorption which Razi et al. implemented [7].

Going one step further, many recent efforts have gone into computational models based on mechanoregulation of e.g. bone fracture healing [67] and (re)modeling [68] in mice, tissue formation in tissue engineered constructs *in vitro* [69,70] or after im-

plantation *in vivo* [71,72]. One known limitation of these *in silico* models is that they usually overestimate targeted (re)modeling, but better approximate the experimental data by including non-targeted (re)modeling [73]. Consequently, we conclude that quantitative metrics such as CCR or AUC can be reported and help *in silico* studies investigating mechanoregulation to facilitate future computational research, as they quantify targeted and non-targeted (re)modeling statistically and can thus identify differences between groups.

Using these metrics to quantify mechanoregulation, it is possible to compare different groups, loading conditions or pharmacological treatments and their influences on the bone response *in vivo*. Combined with our volumetric method, such an analysis in bone tissue engineering would open new horizons regarding investigation and quantification of mechanoregulation in different experimental setups, such as culture conditions and materials, and bone diseases. Moreover, it can help optimize culture duration and cost and affect and improve the computational efforts to optimize scaffold design parameters for bone tissue engineering. This might be especially relevant in the field of rare diseases, where personalized disease models to investigate patho-mechanisms to improve treatment options are of high importance.

5. Conclusion

In conclusion, we were able to demonstrate the presence of mechanoregulation of bone formation in tissue engineered constructs using a volumetric method based on time-lapsed micro-computed tomography and finite element analysis. We quantified mechanoregulation of bone formation in *in vitro* bone scaffolds and showed that dynamic compressive loading increases it in osteogenic medium. Additionally, the method is applicable for the assessment of mechanoregulation in *in vivo* data. This method not only enables the investigation of mechanoregulation in bone scaffolds under different mechanical and biochemical conditions, but will also shed light on the mechanisms driving bone formation in tissue engineered constructs, and finding optimal geometrical parameters and material properties to accelerate culture duration, and thus increase research output as well as decrease therapy development costs.

Declaration of competing interest

The authors declare that they have no known competing financial interests or personal relationships that could have appeared to influence the work reported in this paper.

Supplementary materials

Supplementary material associated with this article can be found, in the online version, at doi:10.1016/j.actbio.2024.03.008.

References

- [1] A. Chekroun, L. Pujo-Menjouet, S. Falcoz, K. Tsuen, K. Yueh-Hsun Yang, J.P. Berteau, Theoretical evidence of osteoblast self-inhibition after activation of the genetic regulatory network controlling mineralization, *J. Theor. Biol.* 537 (2022) 111005, doi:10.1016/j.jtbi.2022.111005.
- [2] J. Waarsing, J. Day, J. van der Linden, A. Ederveen, C. Spanjers, N. De Clerck, A. Sasov, J.A. Verhaar, H. Weinans, Detecting and tracking local changes in the tibiae of individual rats: a novel method to analyse longitudinal *in vivo* micro-CT data, *Bone* 34 (2004) 163–169, doi:10.1016/j.bone.2003.08.012.
- [3] F.A. Schulte, F.M. Lambers, G. Kuhn, R. Müller, *In vivo* micro-computed tomography allows direct three-dimensional quantification of both bone formation and bone resorption parameters using time-lapsed imaging, *Bone* 48 (2011) 433–442, doi:10.1016/j.bone.2010.10.007.
- [4] F.A. Schulte, D. Ruffoni, F.M. Lambers, D. Christen, D.J. Webster, G. Kuhn, R. Müller, Local mechanical stimuli regulate bone formation and resorption in mice at the tissue level, *PLoS ONE* 8 (2013), doi:10.1371/journal.pone.0062172.

- [5] D.C. Tourolle né Betts, E. Wehrle, G.R. Paul, G.A. Kuhn, P. Christen, S. Hofmann, R. Müller, The association between mineralised tissue formation and the mechanical local *in vivo* environment: time-lapsed quantification of a mouse defect healing model, *Sci. Rep.* 10 (2020) 1–10, doi:10.1038/s41598-020-57461-5.
- [6] A.C. Scheuren, P. Vallaster, G.A. Kuhn, G.R. Paul, A. Malhotra, Y. Kameo, R. Müller, Mechano-regulation of trabecular bone adaptation is controlled by the local *in vivo* environment and logarithmically dependent on loading frequency, *Front. Bioeng. Biotechnol.* 8 (2020) 1–13, doi:10.3389/fbioe.2020.566346.
- [7] H. Razi, A.I. Birkhold, R. Weinkamer, G.N. Duda, B.M. Willie, S. Checa, Aging leads to a dysregulation in mechanically driven bone formation and resorption, *J. Bone Miner. Res.* 30 (2015) 1864–1873, doi:10.1002/jbmr.2528.
- [8] P. Christen, K. Ito, R. Ellouz, S. Boutour, E. Sornay-Rendu, R.D. Chapurlat, B. Van Rietbergen, Bone remodelling in humans is load-driven but not lazy, *Nat. Commun.* 5 (2014) 1–5, doi:10.1038/ncomms5855.
- [9] M. Walle, F.C. Marques, N. Ohs, M. Blauth, R. Müller, C.J. Collins, Bone mechanoregulation allows subject-specific load estimation based on time-lapsed micro-CT and HR-pQCT *in vivo*, *Front. Bioeng. Biotechnol.* 9 (2021), doi:10.3389/fbioe.2021.677985.
- [10] P. Christen, K. Ito, A.A. dos Santos, R. Müller, Bert van Rietbergen, Validation of a bone loading estimation algorithm for patient-specific bone remodelling simulations, *J. Biomech.* 46 (2013) 941–948, doi:10.1016/j.jbiomech.2012.12.012.
- [11] C.J. Collins, P.R. Atkins, N. Ohs, M. Blauth, K. Lippuner, R. Müller, Clinical observation of diminished bone quality and quantity through longitudinal HR-pQCT-derived remodeling and mechanoregulation, *Sci. Rep.* 12 (2022) 1–13, doi:10.1038/s41598-022-22678-z.
- [12] J. Zhang, E. Wehrle, M. Rubert, R. Müller, 3D bioprinting of human tissues: biofabrication, bioinks, and bioreactors, *Int. J. Mol. Sci.* (2021) 22, doi:10.3390/ijms22083971.
- [13] G.N. Schädli, J.R. Vetsch, R.P. Baumann, A.M. de Leeuw, E. Wehrle, M. Rubert, R. Müller, Time-lapsed imaging of nanocomposite scaffolds reveals increased bone formation in dynamic compression bioreactors, *Commun. Biol.* 4 (2021) 110, doi:10.1038/s42003-020-01635-4.
- [14] B.W.M. de Wildt, R. van der Meijden, P.A.A. Bartels, N.A.J.M. Sommerdijk, A. Akiva, K. Ito, S. Hofmann, Bioinspired silk fibroin mineralization for advanced *in vitro* bone remodeling models, *Adv. Funct. Mater.* (2022) 32, doi:10.1002/adfm.202206992.
- [15] B.W.M. de Wildt, E.E.A. Cramer, L.S. de Silva, K. Ito, D. Gawlitta, S. Hofmann, Evaluating material-driven regeneration in a tissue engineered human *in vitro* bone defect model, *Bone* 166 (2023) 116597, doi:10.1016/j.bone.2022.116597.
- [16] J.C. Reichert, A. Cipitria, D.R. Epari, S. Saifzadeh, P. Krishnakanth, A. Berner, M.A. Woodruff, H. Schell, M. Mehta, M.A. Schuetz, G.N. Duda, D.W. Huttmacher, A tissue engineering solution for segmental defect regeneration in load-bearing long bones, *Sci. Transl. Med.* 4 (2012) 1–11, doi:10.1126/scitranslmed.3003720.
- [17] J.J. Li, C.R. Dunstan, A. Entezari, Q. Li, R. Steck, S. Saifzadeh, A. Sadeghpour, J.R. Field, A. Akey, M. Vielreicher, O. Friedrich, S.I. Roohani-Esfahani, H. Zreiqat, A novel bone substitute with high bioactivity, strength, and porosity for repairing large and load-bearing bone defects, *Adv. Healthc. Mater.* 8 (2019) 1–14, doi:10.1002/adhm.201801298.
- [18] B. Zhang, J.D. Skelly, J.R. Maalouf, D.C. Ayers, J. Song, Multifunctional scaffolds for facile implantation, spontaneous fixation, and accelerated long bone regeneration in rodents, *Sci. Transl. Med.* 11 (2019) 1–14, doi:10.1126/scitranslmed.aau7411.
- [19] J. Zhang, E. Wehrle, P. Adamek, G.R. Paul, X.H. Qin, M. Rubert, R. Müller, Optimization of mechanical stiffness and cell density of 3D bioprinted cell-laden scaffolds improves extracellular matrix mineralization and cellular organization for bone tissue engineering, *Acta Biomater.* 114 (2020) 307–322, doi:10.1016/j.actbio.2020.07.016.
- [20] J. Zhang, H. Eiyosylu, X. Qin, M. Rubert, R. Müller, 3D bioprinting of graphene oxide-incorporated cell-laden bone mimicking scaffolds for promoting scaffold fidelity, osteogenic differentiation and mineralization, *Acta Biomater.* 121 (2021) 637–652, doi:10.1016/j.actbio.2020.12.026.
- [21] J. Zhang, J. Griesbach, M. Ganeyev, A.K. Zehnder, P. Zeng, G.N. Schädli, A. De Leeuw, Y. Lai, M. Rubert, R. Müller, Long-term mechanical loading is required for the formation of 3D bioprinted functional osteocyte bone organoids, *Biofabrication* (2022) 14, doi:10.1088/1758-5090/ac73b9.
- [22] A.L. Bredenoord, H. Clevers, J.A. Knoblich, Human tissues in a dish: the research and ethical implications of organoid technology, *Science* (2017) 355, doi:10.1126/science.aaf9414.
- [23] 2023 Terminus – Americas Conference & Exhibition Boston Marriott Copley place April 11–14, 2023, *Tissue Eng. Part A* 29 (2023), doi:10.1089/ten.tea.2023.29041.abstracts.
- [24] M. Sun, G. Chi, P. Li, S. Lv, J. Xu, Z. Xu, Y. Xia, Y. Tan, J. Xu, L. Li, Y. Li, Effects of matrix stiffness on the morphology, adhesion, proliferation and osteogenic differentiation of mesenchymal stem cells, *Int. J. Med. Sci.* 15 (2018) 257–268, doi:10.7150/ijms.21620.
- [25] F. Zhao, Y. Xiong, K. Ito, B. van Rietbergen, S. Hofmann, Porous geometry guided micro-mechanical environment within scaffolds for cell mechanobiology study in bone tissue engineering, *Front. Bioeng. Biotechnol.* 9 (2021) 1–10, doi:10.3389/fbioe.2021.736489.
- [26] J.L. Milan, J.A. Planell, D. Lacroix, Computational modelling of the mechanical environment of osteogenesis within a polylactic acid-calcium phosphate glass scaffold, *Biomaterials* 30 (2009) 4219–4226, doi:10.1016/j.biomaterials.2009.04.026.
- [27] C.M. Bidan, K.P. Kommareddy, M. Rumpler, P. Kollmannsberger, P. Fratzl, J.W.C. Dunlop, Geometry as a factor for tissue growth: towards shape optimization of tissue engineering scaffolds, *Adv. Healthc. Mater.* 2 (2013) 186–194, doi:10.1002/adhm.201200159.
- [28] B. De Wildt, K. Ito, S. Hofmann, The impact of culture variables on 3D human *in vitro* bone remodeling: a design of experiments approach, *Adv. Healthc. Mater.* 31 (2022) 1–34.
- [29] M. Brunelli, C.M. Perrault, D. Lacroix, Short bursts of cyclic mechanical compression modulate tissue formation in a 3D hybrid scaffold, *J. Mech. Behav. Biomed. Mater.* 71 (2017) 165–174, doi:10.1016/j.jmbmm.2017.03.008.
- [30] A. Ravichandran, J. Lim, M.S.K. Chong, F. Wen, Y. Liu, Y.T. Pillay, J.K.Y. Chan, S.H. Teoh, *In vitro* cyclic compressive loads potentiate early osteogenic events in engineered bone tissue, *J. Biomed. Mater. Res. Part B* 105 (2017) 2366–2375, doi:10.1002/jbm.b.33772.
- [31] M.M. Saunders, A.F. Taylor, C. Du, Z. Zhou, V.D. Pellegrini, H.J. Donahue, Mechanical stimulation effects on functional end effectors in osteoblastic MG-63 cells, *J. Biomech.* 39 (2006) 1419–1427, doi:10.1016/j.jbiomech.2005.04.011.
- [32] E. Baas, J.H. Kuiper, Y. Yang, M.A. Wood, A.J. El Haj, *In vitro* bone growth responds to local mechanical strain in three-dimensional polymer scaffolds, *J. Biomech.* 43 (2010) 733–739, doi:10.1016/j.jbiomech.2009.10.016.
- [33] S.A.E. Young, M. Rummler, H.M. Taïeb, D.S. Garske, A. Ellinghaus, G.N. Duda, B.M. Willie, A. Cipitria, *In vivo* microCT-based time-lapse morphometry reveals anatomical site-specific differences in bone (re)modeling serving as baseline parameters to detect early pathological events, *Bone* 161 (2022) 116432, doi:10.1016/j.bone.2022.116432.
- [34] S.J.P. Callens, D.C. Tourolle né Betts, R. Müller, A.A. Zadpoor, The local and global geometry of trabecular bone, *Acta Biomater.* 130 (2021) 343–361, doi:10.1016/j.actbio.2021.06.013.
- [35] J.R. Vetsch, D.C. Betts, R. Müller, S. Hofmann, Flow velocity-driven differentiation of human mesenchymal stromal cells in silk fibroin scaffolds: a combined experimental and computational approach, *PLoS ONE* 12 (2017) e0180781, doi:10.1371/journal.pone.0180781.
- [36] L. Pieuchot, J. Marteau, A. Guignandon, T. Dos Santos, I. Brigaud, P.F. Chauvy, T. Cloatre, A. Ponche, T. Petitthory, P. Rougerie, M. Vassaux, J.L. Milan, N. Tusamda Wakhloo, A. Spangenberg, M. Bigerelle, K. Anselme, Curvotaxis directs cell migration through cell-scale curvature landscapes, *Nat. Commun.* 9 (2018), doi:10.1038/s41467-018-06494-6.
- [37] L.F. Bonewald, The amazing osteocyte, *J. Bone Miner. Res.* 26 (2011) 229–238, doi:10.1002/jbmr.320.
- [38] F.A. Schulte, F.M. Lambers, T.L. Mueller, M. Stauber, R. Müller, Image interpolation allows accurate quantitative bone morphometry in registered micro-computed tomography scans, *Comput. Methods Biomech. Biomed. Eng.* 17 (2014) 539–548, doi:10.1080/10255842.2012.699526.
- [39] D.J. Webster, P.L. Morley, H.H. van Lenthe, R. Müller, A novel *in vivo* mouse model for mechanically stimulated bone adaptation – a combined experimental and computational validation study, *Comput. Methods Biomech. Biomed. Eng.* 11 (2008) 435–441, doi:10.1080/10255840802078014.
- [40] F.A. Schulte, A. Zwahlen, F.M. Lambers, G. Kuhn, D. Ruffoni, D. Betts, D.J. Webster, R. Müller, Strain-adaptive in silico modeling of bone adaptation – a computer simulation validated by *in vivo* micro-computed tomography data, *Bone* 52 (2013) 485–492, doi:10.1016/j.bone.2012.09.008.
- [41] F.C. Marques, D. Boaretti, M. Walle, A.C. Scheuren, F.A. Schulte, R. Müller, Mechanostat parameters estimated from time-lapsed *in vivo* micro-computed tomography data of mechanically driven bone adaptation are logarithmically dependent on loading frequency, *Front. Bioeng. Biotechnol.* 11 (2023) 1–23, doi:10.3389/fbioe.2023.1140673.
- [42] D. Webster, F.A. Schulte, F.M. Lambers, G. Kuhn, R. Müller, Strain energy density gradients in bone marrow predict osteoblast and osteoclast activity: a finite element study, *J. Biomech.* 48 (2015) 866–874, doi:10.1016/j.jbiomech.2014.12.009.
- [43] C. Flaig, A Highly Scalable Memory Efficient Multigrid Solver for Micro-Finite Element Analyses, A Highly Scalable Memory Efficient Multigrid Solver for Micro-Finite Element Analyses, 136, 2012, doi:10.3929/ethz-a-007613965.
- [44] W. Pistoia, B. Van Rietbergen, E.M. Lochmüller, C.A. Lill, F. Eckstein, P. Rügsegger, Estimation of distal radius failure load with micro-finite element analysis models based on three-dimensional peripheral quantitative computed tomography images, *Bone* 30 (2002) 842–848, doi:10.1016/S8756-3282(02)00736-6.
- [45] C. Yvanoff, R.G. Willaert, Development of bone cell microarrays in microfluidic chips for studying osteocyte-osteoblast communication under fluid flow mechanical loading, *Biofabrication* (2022) 14, doi:10.1088/1758-5090/ac516e.
- [46] A. Atkins, M.N. Dean, M.L. Habegger, P.J. Motta, L. Ofer, F. Repp, A. Shipov, S. Weiner, J.D. Currey, R. Shahar, Remodeling in bone without osteocytes: bill-fish challenge bone structure-function paradigms, *Proc. Natl. Acad. Sci. U. S. A.* 111 (2014) 16047–16052, doi:10.1073/pnas.1412372111.
- [47] G.R. Paul, P. Vallaster, M. Rüegg, A.C. Scheuren, D.C. Tourolle, G.A. Kuhn, E. Wehrle, R. Müller, Tissue-level regeneration and remodeling dynamics are driven by mechanical stimuli in the microenvironment in a post-bridging loaded femur defect healing model in mice, *Front. Cell Dev. Biol.* 10 (2022) 1–12, doi:10.3389/fcell.2022.856204.
- [48] F.M. Lambers, G. Kuhn, C. Weigt, K.M. Koch, F.A. Schulte, R. Müller, Bone adaptation to cyclic loading in murine caudal vertebrae is maintained with age and directly correlated to the local biomechanical environment, *J. Biomech.* 48 (2015) 1179–1187, doi:10.1016/j.jbiomech.2014.11.020.
- [49] J. Liu, Z. Zhao, J. Li, L. Zou, C. Shuler, Y. Zou, X. Huang, M. Li, J. Wang, Hydrostatic pressures promote initial osteodifferentiation with ERK1/2 not p38

- MAPK signaling involved, *J. Cell. Biochem.* 107 (2009) 224–232, doi:[10.1002/jcb.22118](https://doi.org/10.1002/jcb.22118).
- [50] A. Sittichokechaiwut, J.H. Edwards, A.M. Scutt, G.C. Reilly, Short bouts of mechanical loading are as effective as dexamethasone at inducing matrix production by human bone marrow mesenchymal stem cells, *Eur. Cells Mater.* 20 (2010) 45–57, doi:[10.22203/eCM.v020a05](https://doi.org/10.22203/eCM.v020a05).
- [51] Y. Kameo, T. Adachi, M. Hojo, Transient response of fluid pressure in a poroelastic material under uniaxial cyclic loading, *J. Mech. Phys. Solids.* 56 (2008) 1794–1805, doi:[10.1016/j.jmps.2007.11.008](https://doi.org/10.1016/j.jmps.2007.11.008).
- [52] Y. Kameo, T. Adachi, M. Hojo, Effects of loading frequency on the functional adaptation of trabeculae predicted by bone remodeling simulation, *J. Mech. Behav. Biomed. Mater.* 4 (2011) 900–908, doi:[10.1016/j.jmbbm.2011.03.008](https://doi.org/10.1016/j.jmbbm.2011.03.008).
- [53] S.J. Warden, C.H. Turner, Mechanotransduction in the cortical bone is most efficient at loading frequencies of 5–10Hz, *Bone* 34 (2004) 261–270, doi:[10.1016/j.bone.2003.11.011](https://doi.org/10.1016/j.bone.2003.11.011).
- [54] S.M. Tanaka, K. Tachibana, Frequency-dependence of mechanically stimulated osteoblastic calcification in tissue-engineered bone in vitro, *Ann. Biomed. Eng.* 43 (2015) 2083–2089, doi:[10.1007/s10439-014-1241-z](https://doi.org/10.1007/s10439-014-1241-z).
- [55] K.J. Lewis, D. Frikha-Benayed, J. Louie, S. Stephen, D.C. Spray, M.M. Thi, Z. Seref-Ferlengez, R.J. Majeska, S. Weinbaum, M.B. Schaffler, Osteocyte calcium signals encode strain magnitude and loading frequency *in vivo*, *Proc. Natl. Acad. Sci. U. S. A.* 114 (2017) 11775–11780, doi:[10.1073/pnas.1707863114](https://doi.org/10.1073/pnas.1707863114).
- [56] L. Polo-Corrales, M. Latorre-Esteves, J.E. Ramirez-Vick, Scaffold design for bone regeneration, *J. Nanosci. Nanotechnol.* 14 (2014) 15–56, doi:[10.1166/jnn.2014.9127](https://doi.org/10.1166/jnn.2014.9127).
- [57] M. Kistler-Fischbacher, J.S.S. Yong, B.K. Weeks, B.R. Beck, High-intensity exercise and geometric indices of hip bone strength in postmenopausal women on or off bone medication: the MEDEX-OP randomised controlled trial, *Calcif. Tissue Int.* 111 (2022) 256–266, doi:[10.1007/s00223-022-00991-z](https://doi.org/10.1007/s00223-022-00991-z).
- [58] Z. Li, R. Müller, D. Ruffoni, Bone remodeling and mechanobiology around implants: insights from small animal imaging, *J. Orthop. Res.* 36 (2018) 584–593, doi:[10.1002/jor.23758](https://doi.org/10.1002/jor.23758).
- [59] E.N. Cresswell, M.G. Goff, T.M. Nguyen, W.X. Lee, C.J. Hernandez, Spatial relationships between bone formation and mechanical stress within cancellous bone, *J. Biomech.* 49 (2016) 222–228, doi:[10.1016/j.jbiomech.2015.12.011](https://doi.org/10.1016/j.jbiomech.2015.12.011).
- [60] J.M. Graham, B.P. Ayati, S.A. Holstein, J.A. Martin, The role of osteocytes in targeted bone remodeling: a mathematical model, *PLoS ONE* 8 (2013) 10–14, doi:[10.1371/journal.pone.0063884](https://doi.org/10.1371/journal.pone.0063884).
- [61] D.B. Burr, Targeted and nontargeted remodeling, *Bone* 30 (2002) 2–4, doi:[10.1016/S8756-3282\(01\)00619-6](https://doi.org/10.1016/S8756-3282(01)00619-6).
- [62] A.M. Parfitt, Targeted and nontargeted bone remodeling: relationship to basic multicellular unit origination and progression, *Bone* 30 (2002) 5–7, doi:[10.1016/S8756-3282\(01\)00642-1](https://doi.org/10.1016/S8756-3282(01)00642-1).
- [63] M. Walle, D.E. Whittier, D. Schenk, P.R. Atkins, M. Blauth, P. Zysset, K. Lippuner, R. Müller, C.J. Collins, Precision of bone mechanoregulation assessment in humans using longitudinal high-resolution peripheral quantitative computed tomography *in vivo*, *Bone* 172 (2023) 116780, doi:[10.1016/j.bone.2023.116780](https://doi.org/10.1016/j.bone.2023.116780).
- [64] A. Akiva, J. Melke, S. Ansari, N. Liv, R. Van Der Meijden, M. Van Erp, F. Zhao, M. Stout, W.H. Nijhuis, C. De Heus, C.M. Ortera, J. Fermie, J. Klumperman, K. Ito, N. Sommerdijk, S. Hofmann, An organoid for woven bone, *Adv. Func. Mater.* 2010524 (2021) 1–9, doi:[10.1002/adfm.202010524](https://doi.org/10.1002/adfm.202010524).
- [65] H.M. Frost, The mechanostat: a proposed pathogenic mechanism of osteoporoses and the bone mass effects of mechanical and nonmechanical agents, *Bone Miner* 2 (1987) 73–85.
- [66] A.I. Birkhold, H. Razi, G.N. Duda, S. Checa, B.M. Willie, Tomography-based quantification of regional differences in cortical bone surface remodeling and mechano-response, *Calcif. Tissue Int.* 100 (2017) 255–270, doi:[10.1007/s00223-016-0217-4](https://doi.org/10.1007/s00223-016-0217-4).
- [67] D. Tourolle, A micro-scale multiphysics framework for fracture healing and bone remodelling, ETH Zürich (2019), doi:[10.3929/ethz-b-000364637](https://doi.org/10.3929/ethz-b-000364637).
- [68] D. Boaretti, F.C. Marques, C. Ledoux, A. Singh, J.J. Kendall, E. Wehrle, G.A. Kuhn, Y.D. Bansod, F.A. Schulte, R. Müller, Trabecular bone remodeling in the aging mouse : a *in silico* model using single-cell mechanomics, *Front. Bioeng. Biotechnol.*, (2023) 1–18, doi:[10.3389/fbioe.2023.1091294](https://doi.org/10.3389/fbioe.2023.1091294).
- [69] D.P. Byrne, D. Lacroix, J.A. Planell, D.J. Kelly, P.J. Prendergast, Simulation of tissue differentiation in a scaffold as a function of porosity, Young's modulus and dissolution rate: application of mechanobiological models in tissue engineering, *Biomaterials* 28 (2007) 5544–5554, doi:[10.1016/j.biomaterials.2007.09.003](https://doi.org/10.1016/j.biomaterials.2007.09.003).
- [70] J.L. Milan, J.A. Planell, D. Lacroix, Simulation of bone tissue formation within a porous scaffold under dynamic compression, *Biomech. Model. Mechanobiol.* 9 (2010) 583–596, doi:[10.1007/s10237-010-0199-5](https://doi.org/10.1007/s10237-010-0199-5).
- [71] H. Khayyeri, S. Checa, M. Tägil, F.J. O'Brien, P.J. Prendergast, Tissue differentiation in an *in vivo* bioreactor: *in silico* investigations of scaffold stiffness, *J. Mater. Sci. Mater. Med.* 21 (2010) 2331–2336, doi:[10.1007/s10856-009-3973-0](https://doi.org/10.1007/s10856-009-3973-0).
- [72] M. Jaber, P.S.P. Poh, G.N. Duda, S. Checa, PCL strut-like scaffolds appear superior to gyroid in terms of bone regeneration within a long bone large defect: an *in silico* study, *Front. Bioeng. Biotechnol.* 10 (2022) 1–15, doi:[10.3389/fbioe.2022.995266](https://doi.org/10.3389/fbioe.2022.995266).
- [73] M. Huo, S. He, Y. Zhang, Y. Feng, J. Lu, Simulation on bone remodeling with stochastic nature of adult and elderly using topology optimization algorithm, *J. Biomech.* 136 (2022) 111078, doi:[10.1016/j.jbiomech.2022.111078](https://doi.org/10.1016/j.jbiomech.2022.111078).